Development of a Geomechanics Program for Wellbore Stability Analysis

Saeidi, Omid; Dalkhani, Amin Rahimi

DOI
10.1061/IJGNAI.GMENG-8733

Publication date
2023

Document Version
Final published version

Published in
International Journal of Geomechanics

ASCE

Development of a Geomechanics Program for Wellbore Stability Analysis

Omid Saeidi[1] and Amin Rahimi Dalkhani[2]

Abstract: A geomechanics program for wellbore stability analysis has been developed consisting of two modules: an analytical-based solution and a numerical-based solution. In the first part, input data are imported, including petrophysical well logs, pressure data, formation well tops, and a well path. Lithology intervals are set with proper prediction equations to calculate rock mechanical properties based on laboratory tests. In-situ stress and pore pressure are determined using different methods, including the poroelastic plane strain model and stress polygon. From the theory of plane strain, new equations are solved to determine horizontal tectonic strains (ε_h, ε_H) from drilling events such as total mud loss and breakout during drilling. Safe mud weight bounds are calculated through depth and in different azimuths and inclinations applying the Mohr–Coulomb and the Mogi–Coulomb failure criteria. The latter underestimated the minimum mud weight to prevent wellbore breakout. The transversely vertical isotropy of shale formation is programmed with multiple stress transformations via the weak-plane method. In the second module, a 3D model around the wellbore is discretized with hexahedral eight-point elements and programmed using the finite-element (FE) method. Rock mechanical property and displacement boundary conditions are applied to solve FE equations. Stress from the numerical model matched to the Kirsch model and results show that maximum stress concentration around the wellbore corresponds to the wellbore breakout, which has analytically been established. A new well plan across the 3D model was examined to obtain the safe mud weight bounds and results were in agreement with the analytical calculations. **DOI: 10.1061/IJGNAI.GMENG-8733**. © *2023 American Society of Civil Engineers*.

Author keywords: Mud weight; In-situ stress; Transversely isotropy; Failure criterion; Finite-element analysis; Boundary condition; Mechanical property.

Introduction

Wellbore instabilities during drilling are time-consuming and costly for drilling operation, reservoir completion, and production in the earth energy industry. Today, geomechanical wellbore stability analysis is essential prior to any drilling operation and at the final production stage, such as open-hole completion. In this regard, available data during and after drilling, including well logs, pressure data, drilling tests and evidence, and geological information, are combined to conduct wellbore stability analysis using analytical and numerical solutions. The problems with wellbore instability often involve equivalent mud weight (EMW) both static and dynamic, in-situ stress, formation anisotropy, wellbore direction, pore pressure, and thermal–chemical reaction (Chen et al. 2008; Ma and Chen 2015).

Zoback et al. (2003) studied in-situ stress orientation and magnitude in deep wells in several oilfields. They used the Anderson and Coulomb theories to constrain stress magnitude using the concept of stress polygon. In addition, they incorporated complementary data (Leak-off tests, wellbore breakout, and drilling-induced tensile fractures) from drilled wells, including well test data and geophysical logs to obtain mud weight bounds in different azimuth and inclination of the wellbore. Safe mud weight bounds for wellbore drilling have been calculated substituting induced stresses around wellbore with six permutations using the Mohr–Coulomb failure criterion (Fjaer et al. 2008). The Mohr–Coulomb criterion ignores the middle principal stress then overestimates the mud weight bounds. The effect of middle principal stress (σ_2) on the rock failure has been incorporated in the Mogi–Coulomb criterion, indicating shear failure along an octahedral plane under mean normal stress (Al-Ajmi and Zimmerman 2006). Kidambi and Kumar (2016) built a 1D geomechanical model for a vertical wellbore. They presented calculations for the horizontal tectonic strains and obtained the safe mud weight bounds in a wellbore. However, the theoretical background for horizontal strains calculations has not been mentioned.

Wellbore instability problems commonly in shale formation occur due to shear failure along the weak planes (Jaeger 1960; Wu et al. 2005). Lee et al. (2012) developed a program to solve formation anisotropy using the Mohr–Coulomb failure criterion in a weak plane. They projected in-situ stress on the weak plane using multiple transformation matrices. They applied intact and rock mass properties of transversely isotropic formation to determine safe mud weight for drilling. Liu et al. (2016) presented a wellbore stability model for transversely isotropic shale and determined critical mud weight for stable horizontal drilling by applying the Mohr–Coulomb criterion both in the rock matrix and along the weak planes. They concluded that the horizontal wellbore in shale is more stable when the dip angle of the weak plane is 30°−60° and the dip direction is 0–120°. Setiawan and Zimmerman (2018) used the Lekhnitskii–Amadei solution to calculate the stress and elastic anisotropy in a shale formation and combined the Mogi–Coulomb failure criterion with the weak-plane theory of Jaeger to determine the breakout pressure. They determined the elastic matrix of the anisotropic shale by the generalized plane strain concept and the

[1]Geomechanics Dept., Iranian Offshore Oil Company, Tehran, Iran (corresponding author). Email: o.saeidi@yahoo.com

[2]Dept. of Geoscience and Engineering, Delft Univ. of Technology, Delft, Netherlands. Email: a.rahimidalkhani@tudelft.nl

Note. This manuscript was submitted on December 21, 2022; approved on February 28, 2023; published online on May 22, 2023. Discussion period open until October 22, 2023; separate discussions must be submitted for individual papers. This paper is part of the ***International Journal of Geomechanics***, © ASCE, ISSN 1532-3641.

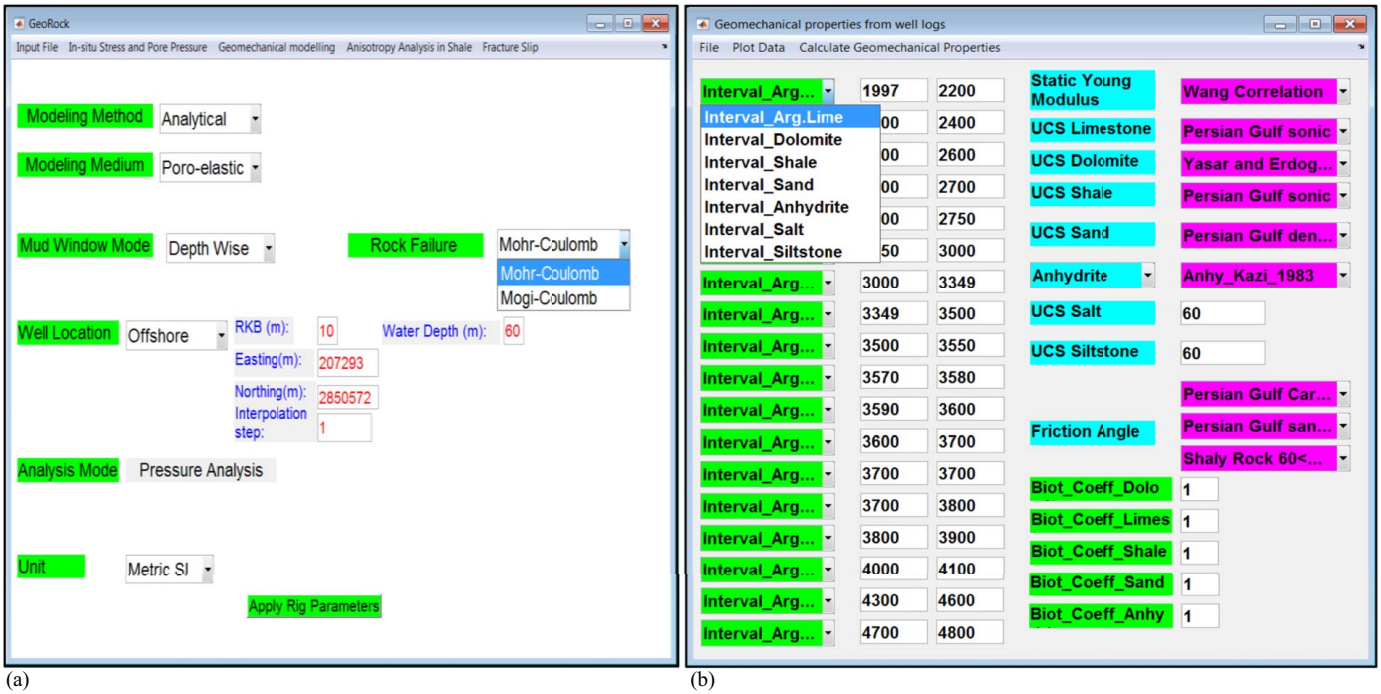

Fig. 1. (a) Opening window with default values; and (b) geomechanical properties in different formation intervals by specific prediction correlations applied from the laboratory tests and literature.

Lekhnitskii method then solved the Beltrami–Michell's stress equations of equilibrium to obtain the stress tensor around a wellbore penetrating a transversely isotropic shale. Their results showed that a highly anisotropic rock implies higher stress concentration. By comparing this with an isotopic rock, the difference could reach approximately 25% for the highest degree of anisotropy. Their results with the Mogi–Coulomb criterion considering the middle principal stress reduced breakout mud pressure with respect to the Mohr–Coulomb criterion.

Asaka and Holt (2021) computed mud weight bounds in a shale formation using the Amadei solution of stress concentration and the Skempton's parameter for induced pore pressure around a wellbore. They found that induced pore pressure based on anisotropy in the Skempton's parameter plays an important role in stress concentration around the wellbore. In low inclination wellbores with high horizontal stress difference, the elastic anisotropy computations give a wider mud weight bounds. Slip along an arbitrary plane due to acting principal stress has been evaluated using the 3D Mohr diagram. This diagram shows discontinuity planes with a pole representing shear and normal stresses acting on it through stress transformation tensors. Xu et al. (2010) analyzed the 3D Mohr diagram to determine pre-existing plane reactivation under stress changes. They found that pre-existing plane reactivation depends on both the maximum stress difference and the middle principal stress. However, they have not considered the effect of pore pressure on the Mohr diagram. Numerical simulation is useful for predicting earth response under different stress and thermal and fluid flow conditions with operational disturbance via drilling. Hawkes et al. (2002) applied an elastoplastic model to simulate medium behavior around the wellbore when reaching a critical stress limit. They concluded that going over the critical stress limit, in this case, does not mean that the rock mass has completely failed, separated, or collapsed. In contrast, it means that the medium can absorb more stresses and accept more deformation. Elyasi and Goshtasbi (2015) used the numerical finite difference codes to study the wellbore stability of a horizontal multidrain oil well. They used the Normalized Yielded Zone Area analysis around the wellbore and its branches to optimize mud pressure and plastic deformation inside the wellbore under different earth stress regimes. Ghoreishian Amiri et al. (2017) developed a hybrid numerical model for multiphase fluid flow in a deformable porous medium. They used a control volume-based finite-element method (FEM) that combines the mesh flexibility of the FE with the local conservative characteristic of the finite volume scheme. They found that combining the control volume-based method and Galerkin FEM is more accurate in modeling multiphase flow in the deformable porous media; it has been found that this method preserves the local conservation of mass and is capable of handling complex geometries and heterogeneities. Li et al. (2018) modeled the thermohydromechanical behavior of a transversely isotropic shale formation using the FEM. They showed that thermally induced pore pressure can be developed in the shale with high clay content and tend to the shear plastic yielding of the formation. Their results showed that the isotropic elastic model underestimates the shear yield of shale in comparison with the transversely isotropic model. Li et al. (2022) presented an integrated geomechanics approach to manage wellbore stability in a deep graben formation. They combined geological, seismic, logging, and drilling data to calculate pore pressure and fracture pressure and provided safe mud weight bounds to guide drilling operations in the graben formation. They also established a discrete-element model to analyze the factors affecting wellbore stability and suggested recommendations for drilling in the graben formation.

This study presents the development of a geomechanical program, namely GeoRock, which consists of two modules, analytical and FE numerical solution, which have been programmed using the graphical user interface (GUI) in Matlab (MathWorks 2009). Most of the commands have been written as follows:

uicontrol('style,''background,''white,''position,'[size of tab],'String,' name of a parameter, 'fontsize,'12,{@callback function})

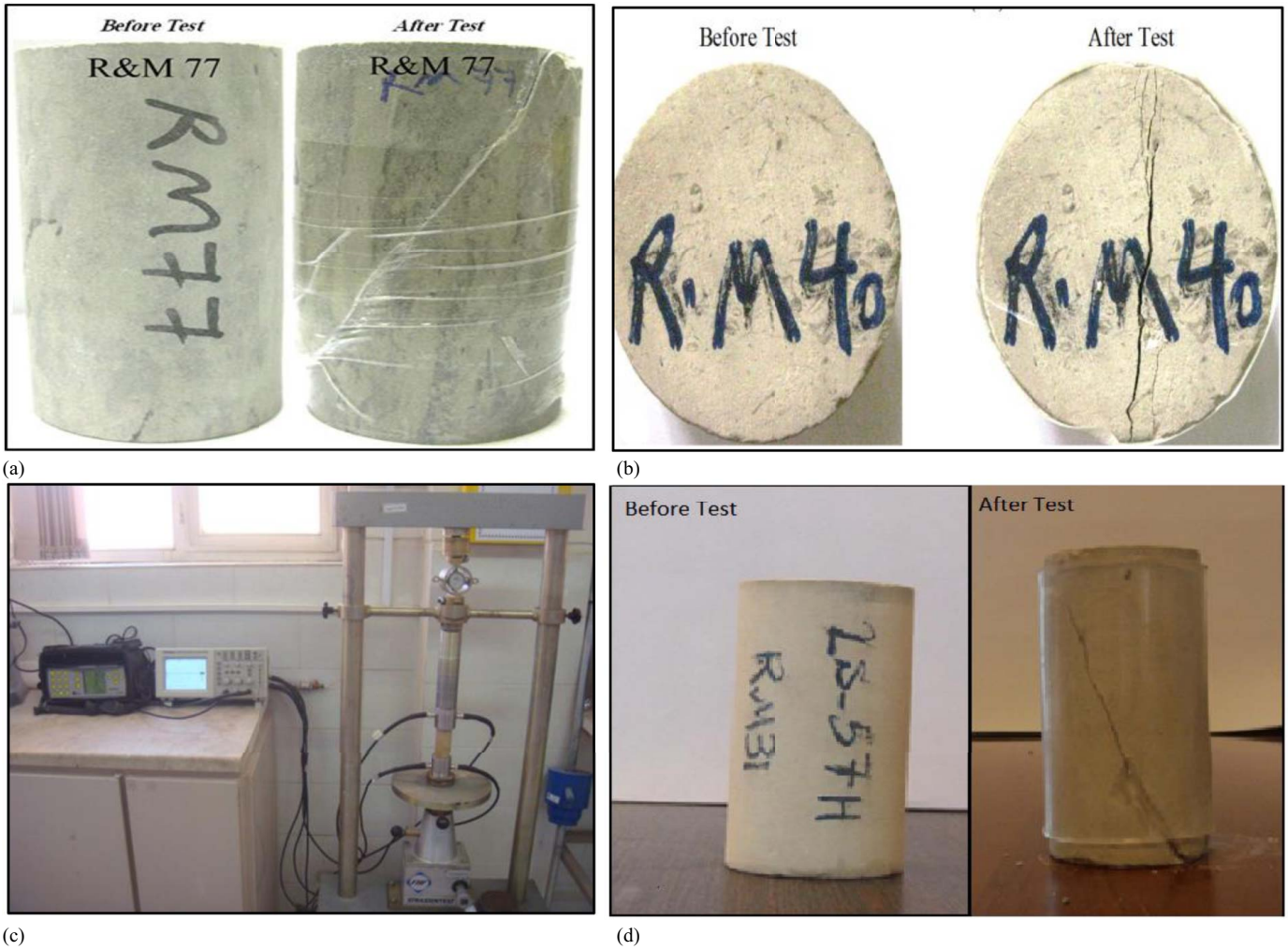

Fig. 2. Mechanical tests on the limestone core specimens ($D = 37.1$ mm, $L = 70.49$): (a) triaxial compression test; (b) Brazilian tensile test ($D = 38.25$ mm, $L = 17.22$ mm); (c) ultrasonic wave velocity measurement; and (d) uniaxial compression test.

The command's properties include "style" as a type of uicontrol such as popup, text, and glider then background color, position, and a callback function. The most common industrial programs are Schlumberger Techlog and Paradigm Geolog. In our program, we also employed transversely isotropic calculation by weak plane concept to determine required mud weight for favorable drilling stability when it comes to fracture slip and a 3D FE analysis module. The analytical module imports input data, and it calculates stable mud weight bounds in different azimuth, inclination, and depth-wise in a wellbore. In the case of minimum data availability, minimum and maximum horizontal strains (ε_h, ε_H) are determined using drilling events such as total mud loss and wellbore breakout by solving plane strain equations. In comparison with those tools, fracture stability analysis of our program provides correct results. Shale's transversely isotropic behavior due to stress or pressure changes is analyzed using stress transformation tensors in arbitrary planes. In the 3D FE part, the wellbore's boundary is discretized with eight-point hexahedral elements. Elements from the global coordinate system are mapped to the natural coordinate system, and a stiffness matrix is calculated in each element by a two-point Gaussian integration rule. Stress tensor and displacement around the wellbore and the entire model are obtained from computations.

Table 1. Prediction correlations for rock properties among well logs and experimental tests

Argillaceous limestone[a]	Limestone	Dolomite	Sandstone/Siltstone[b]
$V_{p\_ult} = 1.12V_p - 628.76$	$UCS = 11.95\ DT^{-0.83}\rho^{5.67}n^{0.15}$	$UCS = 0.4502\rho^{5.2685}$	$UCS = 5 \times 10^{29}e^{-0.75DT}$
$UCS = 0.019V_p - 22.21$	$\varphi = 0.0078V_p - 2.79$	$V_s = 0.2931V_p^{1.0983}$	$V_s = -702.25 + 0.89V_p - 3.95 \times 10^{-5}V_p^2$
$V_s = -602.71 + 0.79V_p\ - 4.95 \times 10^{-5}\ V_p^2$	$T_0 = 0.0014V_p - 0.55$	$\varphi = -0.84DT + 90.122$	$\varphi = 61.71\rho - 117.158$
$E_{st} = 1.76E_{dyn}^{0.5761}$	$E_{st} = 1.28E_{dyn}^{0.6929}$	$T_0 = -0.1127DT + 12.8973$	$T_0 = 0.3UCS$
		$E_{st} = 4.392\ln(E_{dyn}) - 4.192$	$E_{st} = 0.71E_{dyn} + 0.14$

[a]Argillaceous limestone is a rock type with less than 35% clay; V_{p_ult} = ultrasonic p-wave velocity in m/s; V_p and V_s = well log sonic velocity in m/s; UCS = uniaxial compressive strength in MPa; E_{st} = static Young's modulus in GPa; E_{dyn} = dynamic Young's modulus in GPa; DT = sonic slowness in $\mu s/ft$; T_0 = tensile strength in MPa; ϕ = friction angle; ρ = bulk density in g/cm^3; and n = porosity in percentage.
[b]Siltstone is a fine-grained sedimentary rock consisting of more than 50% silt with a diameter of 1/16–1/256 mm.

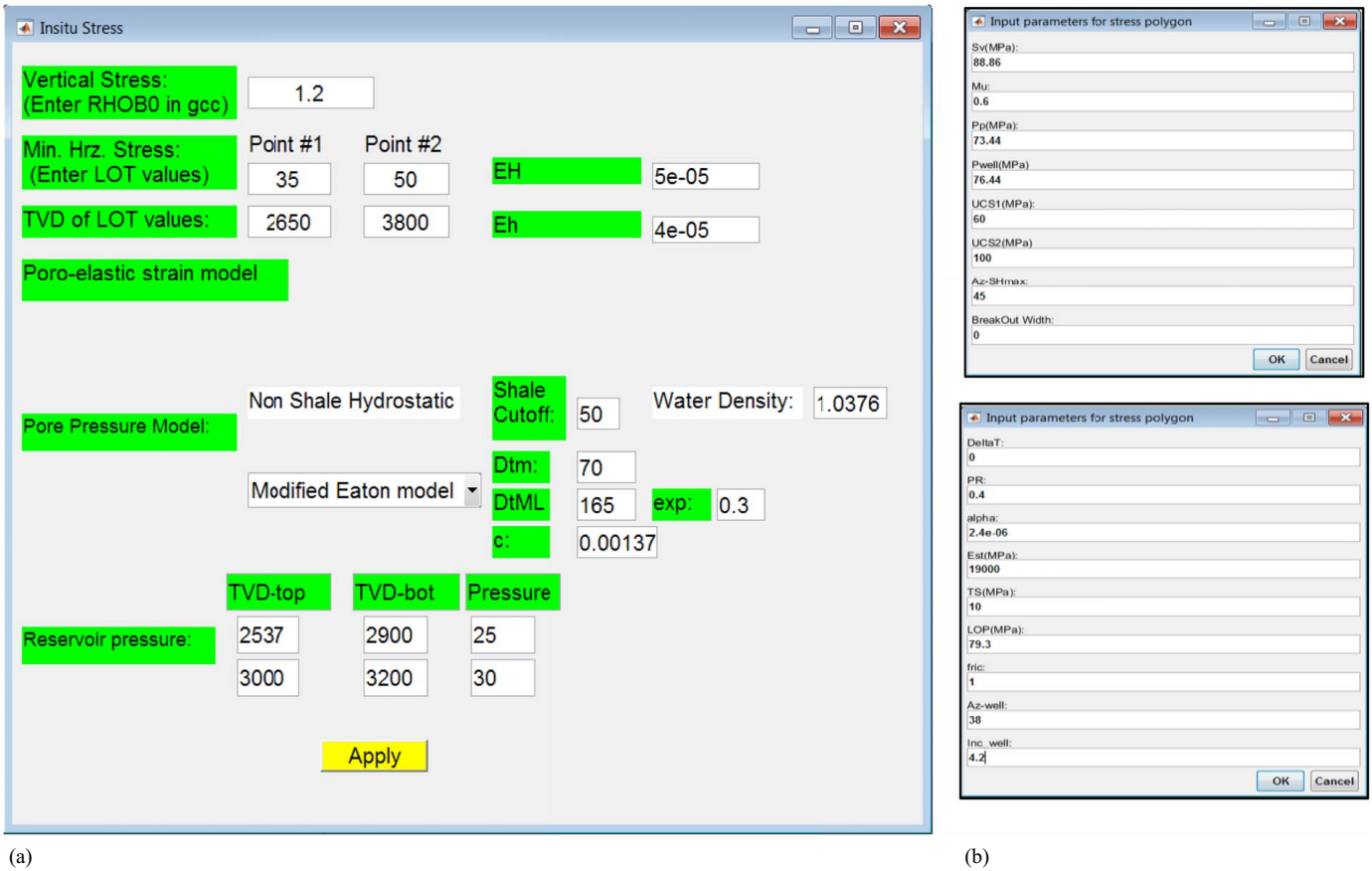

(a) (b)

Fig. 3. (a) In-situ stress and pore pressure calculation by poroelastic strain method; and (b) stress polygon windows with default values.

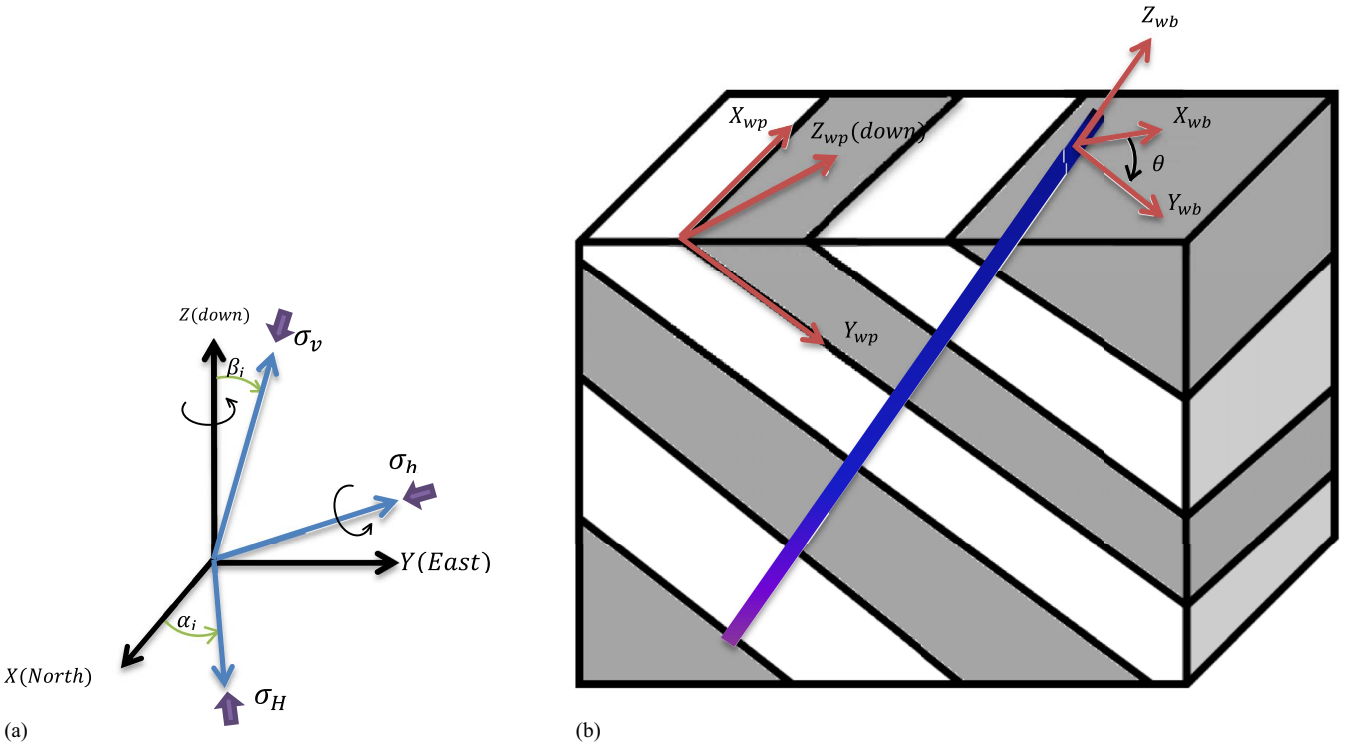

(a) (b)

Fig. 4. (a) Global and local (in-situ stress) coordinate systems; and (b) weak planes in shale, wellbore crossing, and corresponding coordinate systems.

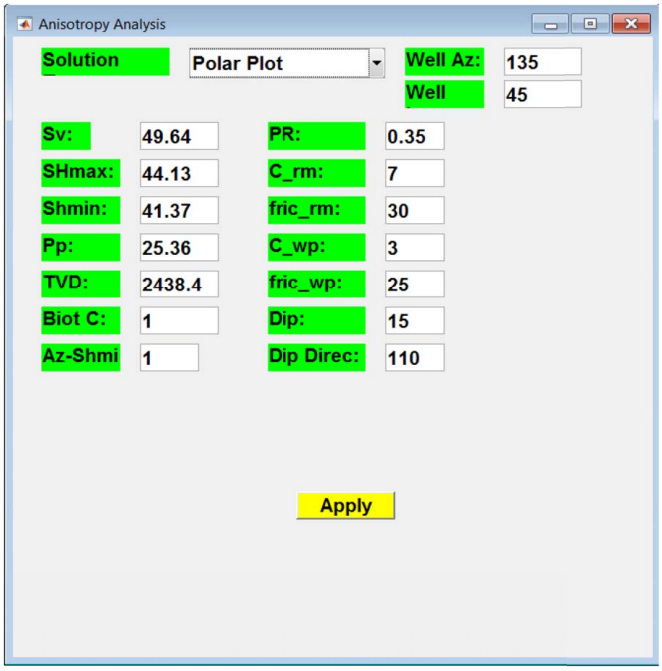

Fig. 5. Data input window to determine breakout mud weight in the anisotropic shale; *C_rm* is intact rock cohesion, *fric_rm* is intact rock friction angle.

Analytical Module

This module imports input data, including petrophysical well logs, pressure data, formation well tops, and well paths. As shown in Fig. 1(a) five main items include input file, in-situ stress pore pressure, and geomechanical modeling in which the final analysis is done to determine safe mud weight bounds; other features include transversely isotropy analysis in shale where the polar plot of mud weight is calculated based on weak-plane theory, and Fracture Slip where a 3D Mohr–Coulomb diagram shows that a fault/fracture to what extent is near to slip due to pore pressure changes. The input file includes seven submenus where for importing raw log data the extensions are Microsoft Excel (.xls, .xlsx) and a standard common LAS (.las) format. Users can independently import calculated rock mechanical properties elsewhere or use the calculate geomechanical properties tab [Fig. 1(b)] to import the well log data and determine rock properties in the specified intervals. Major rock types in our study are: argillaceous limestone, limestone, shale, sandstone, dolomite, anhydrite, and salt. The rock type is selected and the depth interval is entered, then a callback function calculates the geomechanical properties according to the specified rock type and its proper prediction equation.

Rock Mechanical Properties

Seven common rock types in our case, including argillaceous limestone, limestone, shale, sandstone, dolomite, anhydrite, and salt, are added and selected in the specified interval with particular mechanical property correlations from the laboratory rock tests and literature (Eissa and Kazi 1988; Horsrud 2001; Ameen et al. 2009; Fjaer et al. 2008). In order to obtain physiomechanical relations of the recovered rock samples, rock mechanical tests were done on the specimens from several oilfields according to the suggested methods of the International Society for Rock Mechanics (ISRM) as shown in Fig. 2 (ISRM 2007). Thus, both ends of the specimens with $L/D = 2$ were carefully trimmed and polished. Uniaxial compression and triaxial multistage tests were conducted with a loading rate of nearly 1 MPa/s. Ultrasonic P and S wave velocities were measured along and perpendicular to specimens with proper P-polarized and S-polarized transducers. Reliable correlations (R-square > 0.9) among V_{p_ult} and V_{s_ult} from specimens and their corresponding V_p and V_s from the well log were obtained even though the measurement tools are different in the wave's frequency. Table 1 lists prediction correlations between well logs and experimental tests for different rock types implemented in the program.

In-situ Stress and Pore Pressure

Pore pressure in geological formations involves two statuses: normal pressure and abnormal pore pressure. It equals the hydrostatic column of water above a certain point in a normal condition. The mechanisms of abnormal pore pressure (overpressure) include undercompaction, hydrocarbon generation, tectonic compression, and clay mineral digenesis, which many researchers have studied (Gutierrez et al. 2006; Morley et al. 2011; Tingay et al. 2009; Zhang 2011). The most common methods used for pore pressure prediction are Bowers's (Bowers 1995) and Eaton's methods (Eaton 1975). In the first, pore pressure is analyzed based on velocity, density, and resistivity logs reversal, density-velocity cross-plot, and formation loading–unloading due to hydrocarbon generation. In the second, mostly reversal of sonic velocity, porosity, and resistivity logs is used as a tool for overpressure prediction due to undercompaction. Here pore pressure, mostly for shale intervals, is calculated by the modified Eaton's method, which is more applicable for Iranian petroleum basins (Azadpour et al. 2015). On the other side, in nonshale intervals of permeable formations with intragranular connectivity, pressure points of the hydrostatic column can be set.

Principal in-situ stresses are the crucial parameters in geomechanics modeling where different methods can be used for calculation (Molaghab et al. 2017). In the plane strain concept it is assumed that $\varepsilon_z = 0$ but σ_x, σ_y, $\sigma_z \neq 0$ along the wellbore axis. Thus, the principal in-situ stress is expressed as

$$\sigma_x = \frac{E}{(1+\upsilon)(1-2\upsilon)}((1-\upsilon)\varepsilon_x + \upsilon\varepsilon_y) \tag{1}$$

$$\sigma_y = \frac{E}{(1+\upsilon)(1-2\upsilon)}((1-\upsilon)\varepsilon_y + \upsilon\varepsilon_x) \tag{2}$$

$$\sigma_z = \frac{E\upsilon}{(1+\upsilon)(1-2\upsilon)}(\varepsilon_y + \varepsilon_x) \tag{3}$$

where ε_x and ε_y are known as the tectonic strains in petroleum rock mechanics; when rewriting the in-situ stresses like the preceding equations and based on the poroelastic-plane strain concept, they become

$$\sigma_h = \alpha P_p + \frac{\upsilon}{1-\upsilon}(\sigma_v - \alpha P_p) + \frac{E}{(1+\nu)(1-2\upsilon)}((1-\upsilon)\varepsilon_h + \upsilon\varepsilon_H) \tag{4}$$

$$\sigma_H = \alpha P_p + \frac{\upsilon}{1-\upsilon}(\sigma_v - \alpha P_p) + \frac{E}{(1+\nu)(1-2\upsilon)}((1-\upsilon)\varepsilon_H + \upsilon\varepsilon_h) \tag{5}$$

where σ_h = minimum horizontal stress; σ_H = maximum horizontal stress; α = Biot's coefficient; Pp = pore pressure; σ_v = vertical

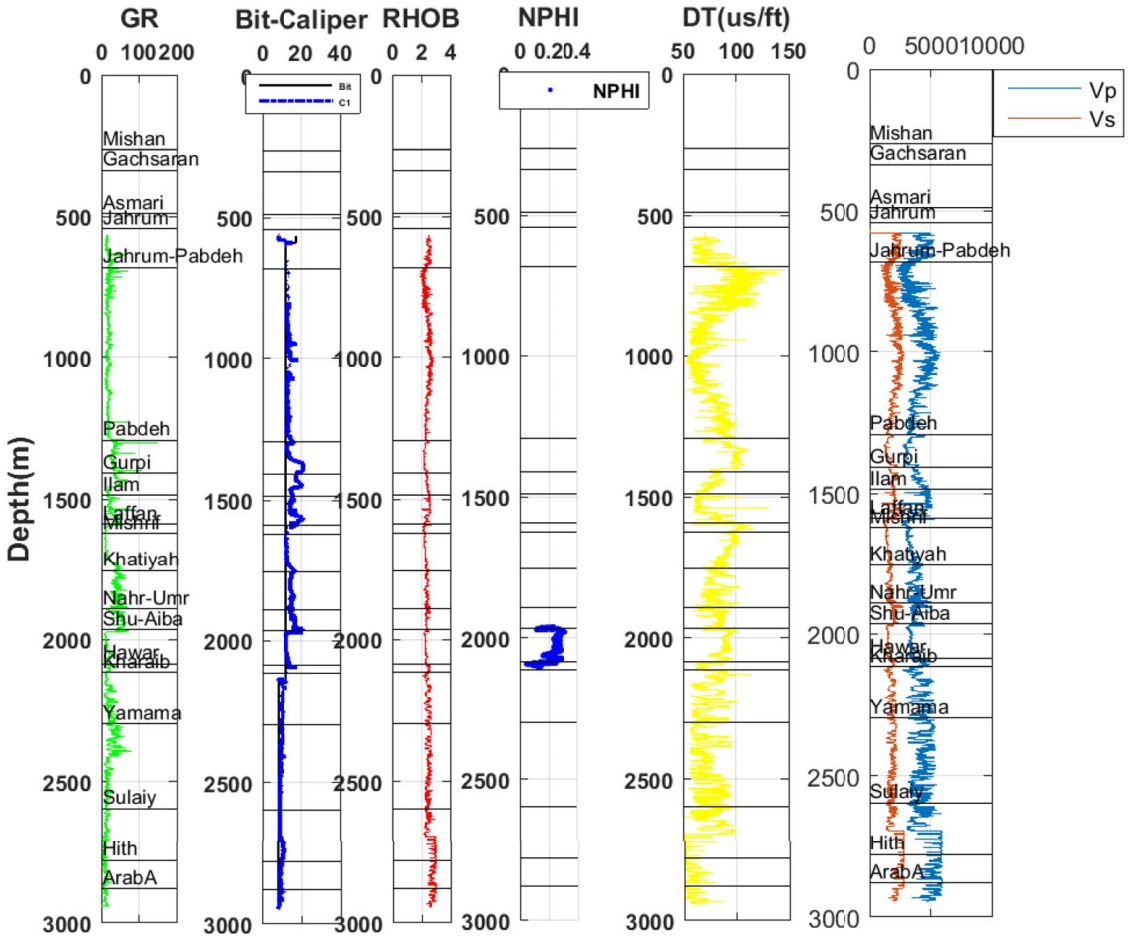

Fig. 6. Imported well logs in which *GR* is Gamma ray, *Bit-Caliper* shows diameter of bit and wellbore, *NPHI* is porosity, *RHOB* is density, *DT* is sonic transit time, V_p and V_s are compressional and shear sonic velocities.

stress; E = Young's modulus; and υ = Poisson's ratio. Conducting an extended leak-off test (XLOT) is important in determining horizontal strains (ε_h, ε_H) in Eqs. (4) and (5). In conventional drilling, drillers usually skip XLOT due to the formation damage, fracturing, and need for a cementing cure followed by operational delays. Thus, here the horizontal strains are constrained by the plane strain equations [Eqs. (1)–(3)], image logs, and drilling events. Drilling events, including total (complete) mud loss (because of induced fracturing not fracture/fault) and wellbore breakout, occur at the maximum and minimum horizontal stress directions, respectively. Therefore, minimum and maximum hoop stress compressions relevant to these stresses around the wellbore from Kirsch equations (Bradley 1979) can be expressed as

$$\sigma_\theta = \sigma_H + \sigma_h - 2(\sigma_H - \sigma_h)\cos 2\theta - Pp - Pw \tag{6}$$

$$3\sigma_h - \sigma_H - Pp - P_{wb} \le -T_0, \quad \theta = 0, \pi \tag{7}$$

$$UCS \ge 3\sigma_H - \sigma_h - Pp - Pw, \quad \theta = \pm\frac{\pi}{2} \tag{8}$$

Assuming $\alpha = 1$ and introducing Eqs. (4) and (5) into Eqs. (7) and (8) and solving the equations gives horizontal strains as

$$(3-4\nu)\varepsilon_h - (1-4\upsilon)\varepsilon_H = \frac{Pp + P_{wb} - T_0 - 2m}{q} \tag{9}$$

$$(3-4\nu)\varepsilon_H - (1-4\upsilon)\varepsilon_h = \frac{Pp + P_w + UCS - 2m}{q}$$
$$q = \frac{E}{(1+\nu)(1-2\upsilon)},\ m = \alpha P_p + \frac{\upsilon}{1-\upsilon}(\sigma_v - \alpha P_p) \tag{10}$$

where ε_h and ε_H = horizontal minimum and maximum strains; Pp = pore pressure; θ is measured from the direction of σ_H; P_{wb} = formation breakdown pressure; UCS = unconfined compressive strength; T_0 = rock tensile strength; P_w = well pressure; and q and m = variables. Most of the time, both induced fracturing and breakout would not happen simultaneously in a well, then the horizontal strains can be calculated from Eqs. (3) and (9) or (10). Fig. 3 shows the window for pore pressure and in-situ stress calculations by the poroelastic strain method [Fig. 3(a)] and the stress polygon method [Fig. 3(b)]. Details of the stress polygon method can be found in Zoback (2007). Here, *RHOB0* denotes density at the surface for onshore wells or the mudline for offshore wells; reservoir pressure points are used for pore pressure calibration, *Mu* is the crustal coefficient of friction, *Az-SHmax* is the azimuth of *SHmax* from north, *DeltaT* is the differential temperature of drilling fluid and formation.

Transversely Vertical Isotropic Shale Formation

Anisotropic formations, mainly shale, due to shear failure along weak planes require a different critical mud window than do the isotropic formations (Lee et al. 2012). In-situ stress must be

Table 2. Formations title and their lithology

Mishan	Gachsaran	Asmari	Jahrum	Jahrum-Pabdeh	Pabdeh	Gurpi	Ilam	Laffan	Mishrif	Nahr-Umr	Shuaiba	Hawar	Kharaib	Yamama	Sulaiy	Hith	Arab
Claystone	Anhydrite	Dolomite	Dolomite	Dolomite + Marl	Marl	Shale	Limestone	Shale	Limestone	Shale	Limestone	Marl	Limestone	Limestone	Dolomite	Anhydrite	Dolomite + Anh.

transformed three times, as shown in Fig. 4, to calculate stress tensor along the weak planes. The first tensor transform is done from the in-situ principal coordinate system to global coordinate the system via rotation α_i around Z-axis and rotation β_i around σ_h-axis, which is expressed as

$$\sigma_{in-gl} = B'\sigma_{in}B \tag{11}$$

$$\sigma_{in} = \begin{bmatrix} \sigma_H & 0 & 0 \\ 0 & \sigma_h & 0 \\ 0 & 0 & \sigma_v \end{bmatrix}, \quad B = \begin{bmatrix} \cos\alpha_i\cos\beta_i & \sin\alpha_i\cos\beta_i & \sin\beta_i \\ -\sin\alpha_i & \cos\alpha_i & 0 \\ -\cos\alpha_i\sin\beta_i & -\sin\alpha_i\sin\beta_i & \cos\beta_i \end{bmatrix} \tag{12}$$

The second tensor transform is done from global to wellbore coordinate system via rotation α_{wb} around Z_{wb}-axis and β_{wb} around Y_{wb}-axis, which is expressed as

$$\sigma_{gl-wb} = T\sigma_{in-gl}T' \tag{13}$$

$$\sigma_{gl-wb} = \begin{bmatrix} \sigma_{xx}^{wb} & \tau_{xy}^{wb} & \tau_{xz}^{wb} \\ \tau_{yx}^{wb} & \sigma_{yy}^{wb} & \tau_{yz}^{wb} \\ \tau_{zx}^{wb} & \tau_{zy}^{wb} & \sigma_{zz}^{wb} \end{bmatrix}, \quad T = \begin{bmatrix} \cos\alpha_{wb}\cos\beta_{wb} & \sin\alpha_{wb}\cos\beta_{wb} & \sin\beta_{wb} \\ -\sin\alpha_{wb} & \cos\alpha_{wb} & 0 \\ -\cos\alpha_{wb}\sin\beta_{wb} & -\sin\alpha_{wb}\sin\beta_{wb} & \cos\beta_{wb} \end{bmatrix} \tag{14}$$

The third tensor transform is done from a global to weak plane coordinate system via rotation α_{wp} around Z_{wp}-axis and β_{wp} around Y_{wp}-axis, which is expressed as

$$\sigma_{wb-wp} = MT'C'\sigma_{ccs}CTM' \tag{15}$$

$$\sigma_{ccs} = \begin{bmatrix} \sigma'_{rr} & \tau_{r\theta} & \tau_{rz} \\ \tau_{r\theta} & \sigma'_{\theta\theta} & \tau_{\theta z} \\ \tau_{rz} & \tau_{\theta z} & \sigma'_{zz} \end{bmatrix} \quad C = \begin{bmatrix} \cos\theta & \sin\theta & 0 \\ -\sin\theta & \cos\theta & 0 \\ 0 & 0 & 1 \end{bmatrix} \tag{16}$$

$$M = \begin{bmatrix} \cos\alpha_{wp}\sin\beta_{wp} & \sin\alpha_{wp}\sin\beta_{wp} & \cos\beta_{wp} \\ -\sin\alpha_{wp} & \cos\alpha_{wp} & 0 \\ -\cos\alpha_{wp}\cos\beta_{wp} & -\sin\alpha_{wp}\cos\beta_{wp} & \sin\beta_{wp} \end{bmatrix} \tag{17}$$

In the preceding equations, σ_{ccs} is the effective stress tensor in a cylindrical coordinate system around the wellbore (Bradley 1979). Fig. 5 shows the data input for breakout mud weight in a shale formation calculated by the preceding procedure [Eqs. (11)–(19)]. Mud weight calculation has been started in a specified azimuth and inclination of the wellbore, with a minimum value of 30 pcf (4 ppg) up to the minimum horizontal stress or the fracture gradient (the upper bound of mud weight window) with the fixed increments based on the preceding procedure program. However, in the overbalanced drilling practice, mud weight could not be less than 56 pcf due to the operational limits even with a high ratio of diesel mixture. The stress tensor is calculated using Eqs. (11)–(17) and two possible failure mechanisms: failure through intact rock matrix and shear failure along the weak plane is established using the Mohr–Coulomb criterion in this program. To check the intact rock failure, σ'_1 and σ'_3, which are the principal effective stresses extracted from σ_{ccs} in Eq. (16), are introduced as

$$\sigma'_1 = UCS + \sigma'_3\tan^2\left(\frac{\varphi}{2} + 45\right) \tag{18}$$

If the intact rock fails, the mud weight is stored for this point and proceeds to the next wellbore point. The procedure is repeated for checking failure along the weak plane around the wellbore in all directions. By projecting shear stress on the weak plane as in

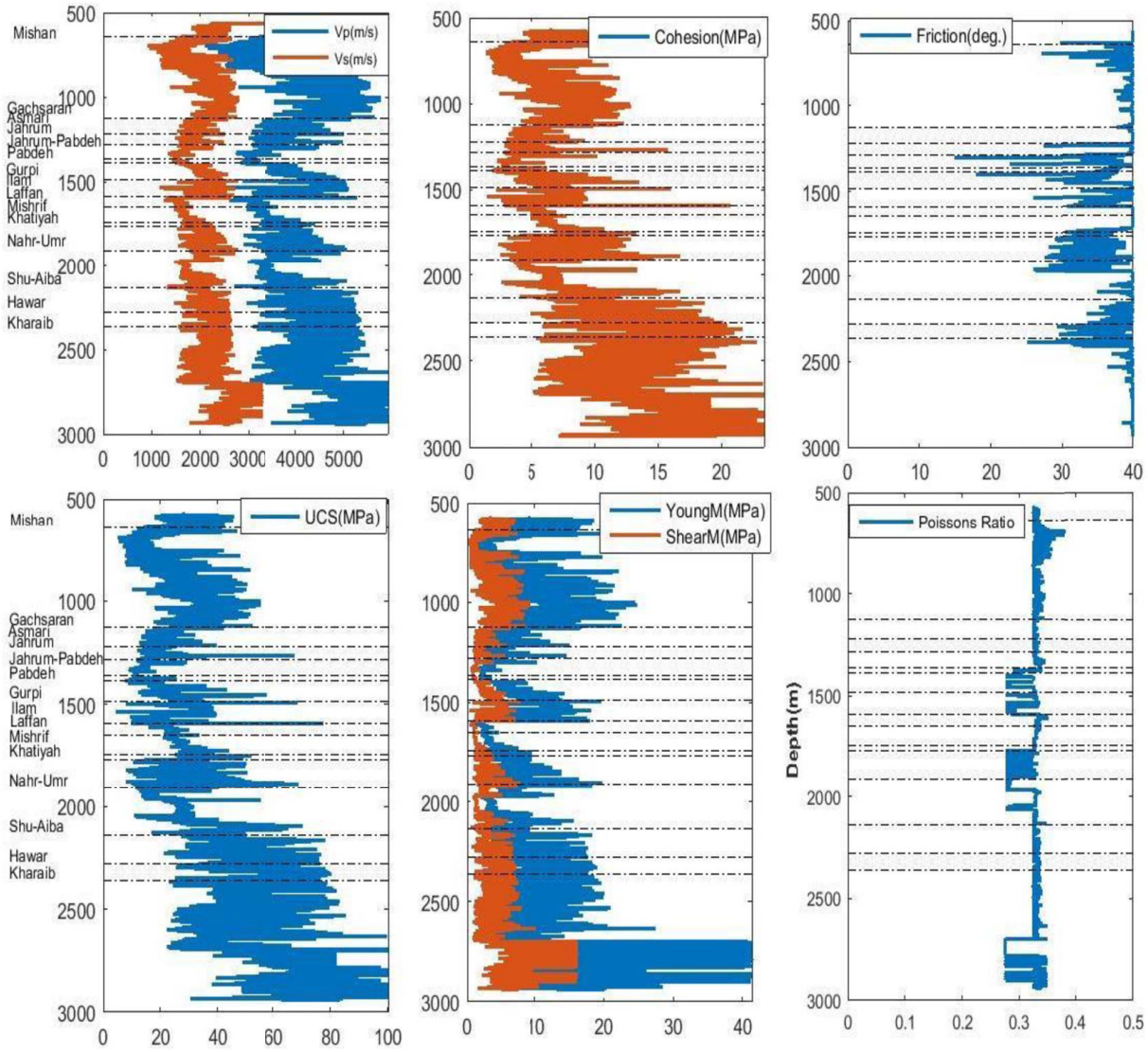

Fig. 7. Rock mechanical properties predicted by the well logs.

Eq. (15), failure occurs when it exceeds normal stress along weak plane according to the Mohr–Coulomb criterion as (Jaeger 1960)

$$\tau_w = C_w + \sigma_{nw}\tan(\varphi_w)$$
$$|\tau_w| = \sqrt{\tau_{xy}^2 + \tau_{xz}^2} \quad (19)$$

where τ_w, σ_{nw}, C_w, and φ_w = shear stress, normal stress, cohesion, and friction angle across the weak plane. Breakout mud weight is the maximum of intact rock and weak plane mud weight at each point.

Field Data for the Wellbore Stability Analysis

To proceed with the first module, which also called 1D geomechanical model or wellbore stability analysis, actual data from a wellbore, including well logs are imported, as shown in Fig. 6. The lithology in the analyzed formations is listed in Table 2. Rock mechanical properties calculated from prediction correlations as described in the section "Rock Mechanical Properties" are shown in Fig. 7. It is not possible to core the whole geological intervals for the laboratory tests; thus predicted results mostly from well logs can be corrected based on the drilling evidence such as tight holes, stuck pipes, mud losses, and particularly with a caliper and image log that shows wellbore breakout or drilling-induced fractures. Fig. 8 shows the calculated pore pressure and in-situ stress in this well based on Eqs. (4) and (5) where the pore pressure has been calibrated with the reservoir drill stem test (DST). As shear sonic is unavailable in this wellbore, parabolic prediction correlations in Table 1 are used to obtain shear velocity (V_s) in each formation. Static Young's modulus is calculated using the conversion of dynamic well log correlations from literature (Elkatatny et al. 2018) as

$$\ln(E_{st}) = 14.9 - 0.61\ln(DT) - 2.18\ln(DTS) + 1.42\ln(\rho) \quad (20)$$

where DTS = shear sonic slowness; and ρ = bulk density.

Given that no clear velocity or density log reversal (Fig. 6) was observed, the modified Eaton's method is used to calculate the pore pressure. Although no LOTs have been conducted, a complete mud loss (>100 barrels/hour) has been reported in this well at 1,152 mMD. At this point the parameters obtained are: P_{wb} = 13.4 MPa, σ_v = 23 MPa, P_p = 10.6 MPa, UCS = 36 MPa, ν = 0.26, E = 19 GPa, and P_w = 11.25 MPa; solving Eqs. (9) and (3) give $\varepsilon_h = -0.00022$ and $\varepsilon_H = 0.00303$, by substituting in Fig. 3

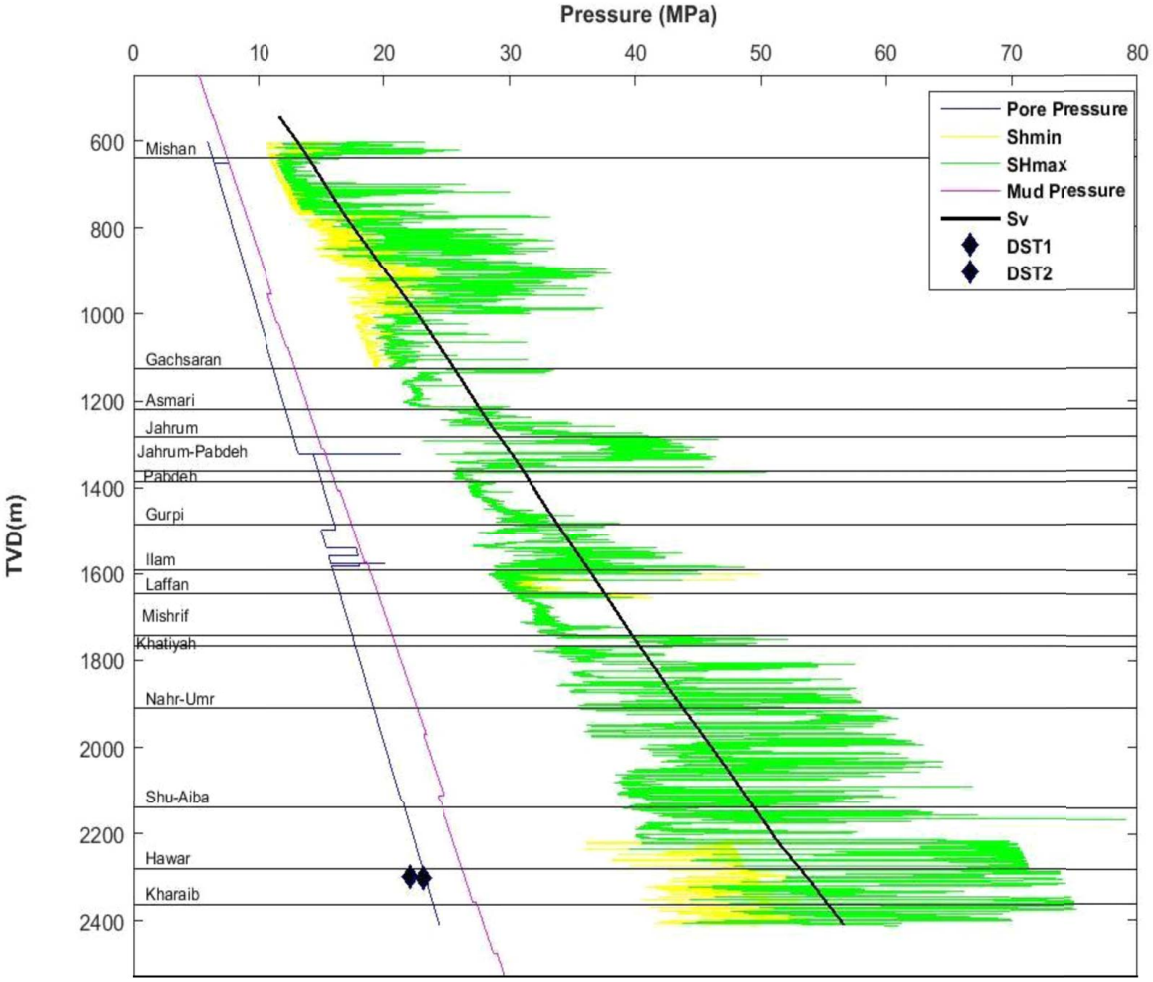

Fig. 8. Pore pressure and in-situ stress from well logs; black diamond points are *DST* measurements.

provides the in-situ stresses as in Fig. 8. The log plot of data shows many fluctuations where there are several methods to find an expected value for each lithology such as smoothing, classification, clustering, and averaging, where in this study we used the average of parameters as listed in Table 3.

Based on the geomechanical properties and in-situ stress calculated in the formations and applying the Mohr–Coulomb and Mogi–Coulomb criteria, the depth-wise mud weight window is depicted in Fig. 9. The theoretical calculations of the mud weight bounds based on the rock failure criteria are presented in Appendix I. The Mogi–Coulomb criterion is popular as it considers the effect of the middle principal stress (σ_2) on the rock shear failure along the octahedral plane (Al-Ajmi and Zimmerman 2006). Here, the breakout mud weight and fracture gradient were calibrated

Table 3. Average of rock physical and mechanical properties

Formation	Depth	P_w	ρ	V_p	V_s	E_{st}	Pp	φ	ν	UCS	σ_h	σ_H	σ_v
Jahrum	541	7	2.495	4,278	2,156	24	5	38	0.22	33	8	20	14
Jah.-Pa.	681	10	2.424	3,890	1,929	21	8	36	0.23	33	13	23	20
Pabdeh	1,271	13	2.260	2,866	1,401	12	13	29	0.34	25	20	25	26
Gurpi	1,376	14	2.339	3,294	1,741	16	13	32	0.31	9	20	28	28
Ilam	1,456	15	2.543	4,594	2,342	27	13	40	0.32	17	22	37	30
Laffan	1,554	16	2.349	3,354	1,815	17	15	32	0.29	11	22	30	31
Mishrif	1,594	17	2.263	2,875	1,410	12	17	31	0.23	32	22	26	33
Khatiyah	1,745	18	2.394	3,607	1,891	18	17	31	0.25	33	23	32	35
Nahr-U	1,899	19	2.358	3,385	1,830	17	18	32	0.29	13	26	34	37
Shuaiba	1,973	20	2.303	3,075	1,598	14	20	32	0.23	26	26	32	39
Hawar	2,086	21	2.513	4,372	2,218	24	19	37	0.22	36	26	38	40
Kharaib	2,113	21	2.452	4,015	2,016	21	20	36	0.23	33	27	38	42
Yamama	2,274	23	2.515	4,440	2,219	25	21	36	0.23	39	30	43	47
Sulaiy	2,542	25	2.430	3,877	1,943	20	24	38	0.23	29	33	43	50
Hith	2,696	27	2.901	7,812	4,212	85	19	52	0.26	88	33	94	52
Arab-A	2,784	28	2.753	6,418	3,199	53	22	48	0.25	48	36	71	55

Note: Depth is in m; ρ = bulk density in g/cm^3; velocities in m/s; E_{st} = static Young's modulus in GPa; pressures and strength in MPa.

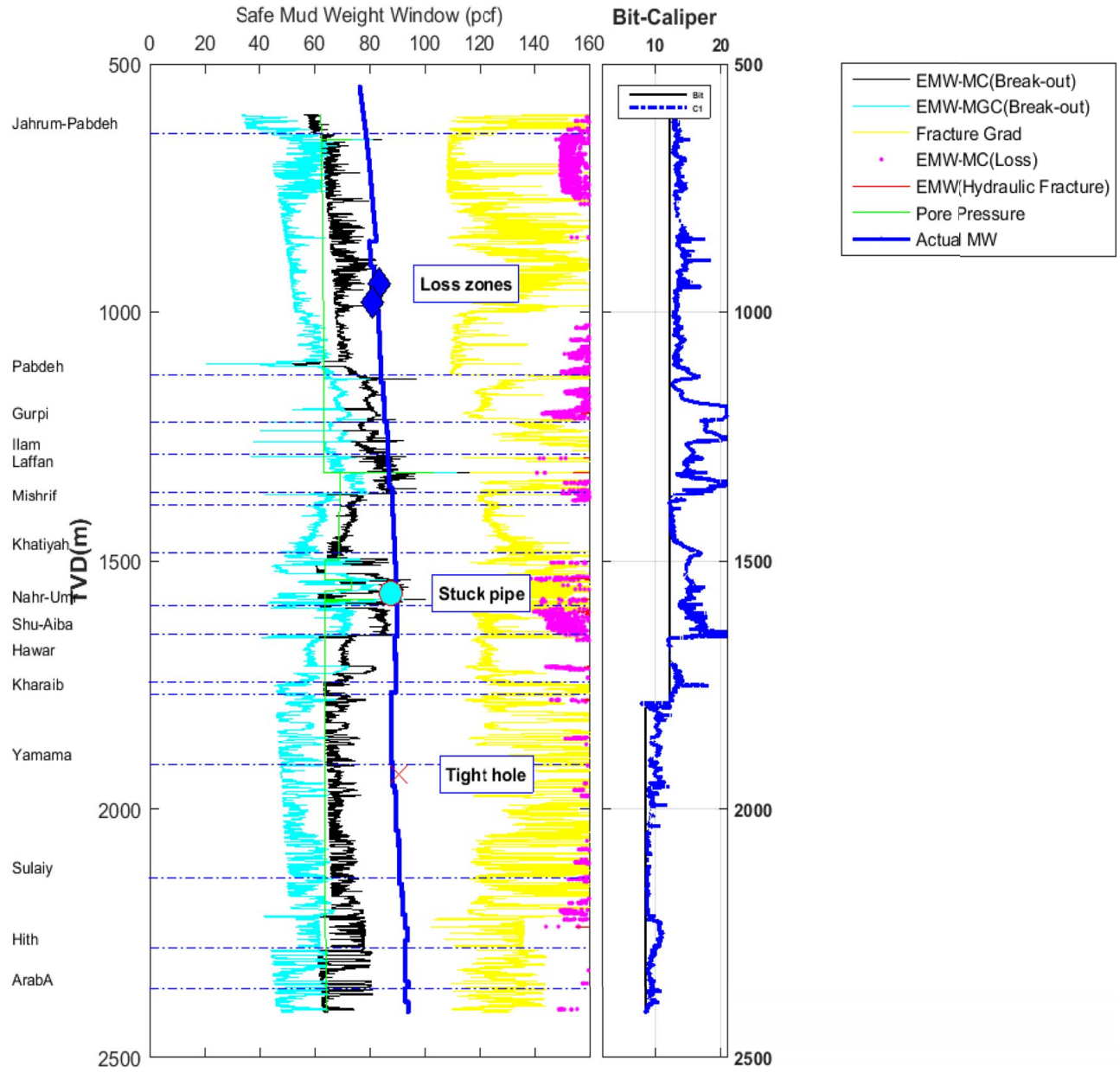

Fig. 9. Mud weight window through depth based on geomechanical properties and in-situ stress in the well; EMW is equivalent mud weight, MC is the Mohr–Coulomb, and MGC is the Mogi–Coulomb EMWs.

with a caliper log, where a stuck pipe and a tight hole at 1,530 and 1,800 m depths, respectively, and mud loss at 800 m were observed that agreed with the wellbore failure while drilling. At the stuck pipe depths, the drill string gets stuck because of formation collapse, showing that the actual mud weight is less than the breakout mud weight; then, mud weight increase is suggested at this interval in the later drilling operations. The Mogi–Coulomb criterion (EMW-MGC) underestimates the breakout mud weight because it is less than the EMW-MC and the pore pressure. Fig. 10 shows the mud weight required to prevent formation collapse and fracturing of the wellbore in different azimuths and inclinations. The EMW of the breakout varies from 69 pcf at the σ_h direction (the stable direction, since it needs less mud weight for retaining the wellbore wall) to 79 pcf at the σ_H direction (the unstable direction, since it needs a higher mud weight). The polar plot is symmetric along both horizontal stresses; however, it could be different in an anisotropic formation such as shale and is discussed later in this section.

Fracture stability analysis in the reservoir is important as it reacts to pressure injection or depletion during development periods of the field. Different types of fractures such as natural fractures, open fractures, and drilling-induced fractures were picked in an OBMI-UBI log after drilling the wellbore and their corresponding effective normal and shear stress have been calculated using the Fracture Slip tab of the program as shown in Fig. 11. Table 4 lists input data of discontinuities that have been picked on the image logs for fracture instability analysis. Shear stress and effective normal stress were calculated by transferring the average of in-situ stress over Yamama interval (Table 3) from the global coordinate system to the fracture plane orientation. Among the fractures, an open fracture at 2,759 m is near to failure envelope, where by pressure injection in the reservoir it is possible to be reactivated and tends to the wellbore failure.

The effect of shale anisotropy on the polar plot of mud weight is determined using the section "Transversely Vertical Isotropic Shale

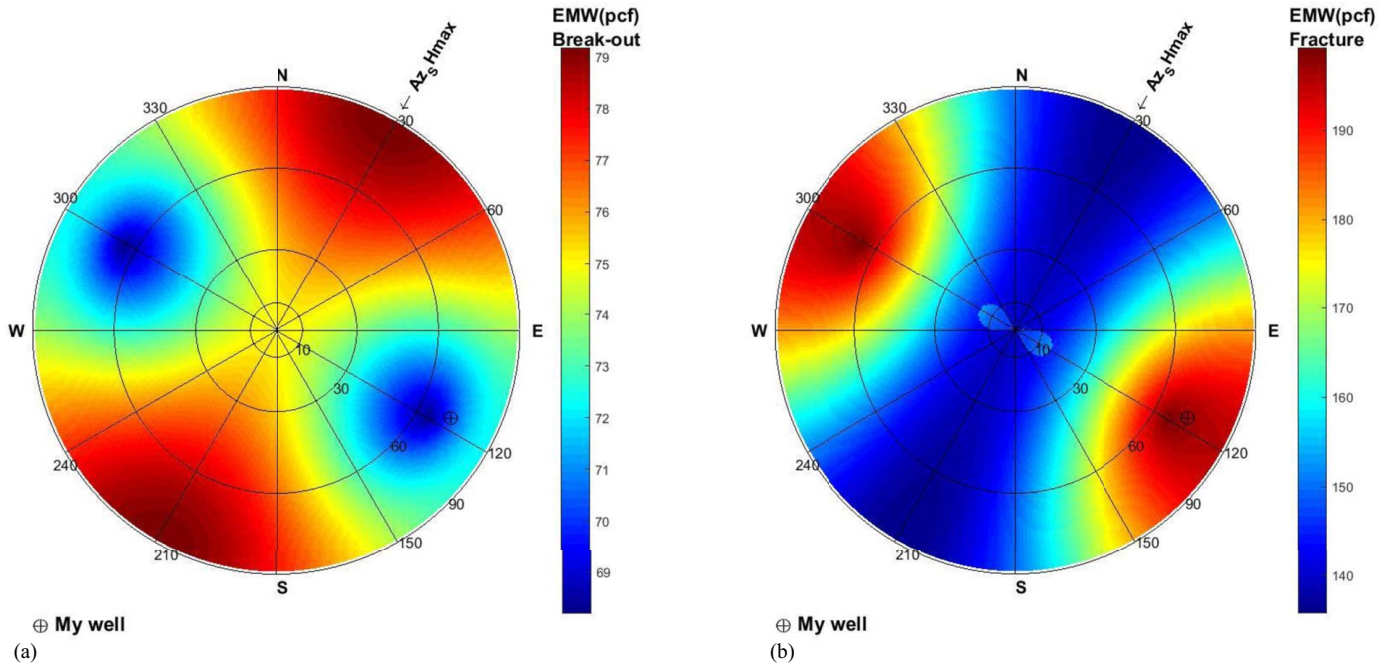

Fig. 10. Polar plots of mud weight: (a) collapse; and (b) induced fracturing mud weight at 1,190 mTVD. Input data include: $\nu = 0.34$; $\phi = 29°$, $UCS =$ 25 MPa, $P_p = 13$ Mpa, $\sigma_v = 26$ MPa, $\sigma_h = 23$ MPa, $\sigma_H = 25$ MPa.

Formation" procedure at 1,363 mTVD, in this case study. As seen in Fig. 12(a), the mud weight plot is no longer symmetric and varies in different azimuth and inclination due to the considering rock anisotropy. In this case, the formation dip is 12° toward the northeast and the direction of σ_h is 120° from the north. It is observed in sensitivity analysis along well inclination [Fig. 12(b)] that wells drilled with an inclination less than 40° and nearly up-dip ($\alpha_{wb} =$ 210°–240°) formation, required a minimum mud weight of 73 pcf concerning other directions; for example, down-dip ($\alpha_{wb} = 30^{\circ}$) and cross-dip ($\alpha_{wb} = 120^{\circ}$).

Numerical Module

A 3D mesh around the wellbore is generated and extended to a depth to form hexahedral eight-point elements in the numerical module. Linear FE is used for computation, and rock material is assumed to be continuous, isotropic, elastic, and homogenous. Stiffness matrices are calculated using the two-point integration Gaussian method in the whole model. The detail of the numerical module is described in the following sections.

Mesh Generation

Grid generation is one of the most important steps in numerical modeling, particularly when the boundary of the problem domain has curvature or bending. A popular method for grid generation is the algebraic transfinite interpolation method. Advantages of grid generation based on interpolation include, first, rapid computation of grids and, second, direct control over grid point locations (Leseikin 2010). The key issue in this method is the blending function in which grid lines at the boundary and internal surfaces are matched. In our model, the first degree of Lagrange polynomial as $1-\xi$, ξ, $1-\eta$ and η are used as blending function and basic transfinite interpolation formula is expressed as

$$X(\xi,\eta) = (1-\eta)X_b(\xi) + \eta X_t(\xi) + (1-\xi)X_l(\eta) + \xi X_r(\eta) - \{\xi\eta X_t(1) + \xi(1-\eta)X_b(1) + \eta(1-\xi)X_t(0) + (1-\xi)(1-\eta)X_b(0)\} \quad (21)$$

where $X =$ blending function in terms of ξ and η axes of logical or computational space, which is mapped to the physical space of the problem; and subscripts b, t, l, and $r =$ bottom, top, left, and right of the domain. Eq. (21) has been used to create four quadrants containing a wellbore cross section along with boundaries that merged to form whole mesh, finally. Fig. 13 shows a bilinear quadratic mesh around the wellbore created using the transfinite interpolation method. Since the wellbore is vertical, it can be extended to hexahedral eight-point (brick element) by adding the Z-location of nodes.

Governing Equations in FE Analysis

In static equilibrium, the rock encounters very slow displacement without motion-like seismic wave propagation; the equations of stress equilibrium are expressed as (Jaeger et al. 2007)

$$\begin{cases} \dfrac{\partial\sigma_x}{\partial x} + \dfrac{\partial\tau_{xy}}{\partial y} + \dfrac{\partial\tau_{xz}}{\partial z} + f_x + \sigma_{x0} = 0 \\ \dfrac{\partial\tau_{yx}}{\partial x} + \dfrac{\partial\sigma_y}{\partial y} + \dfrac{\partial\tau_{yz}}{\partial z} + f_y + \sigma_{y0} = 0 \\ \dfrac{\partial\tau_{zx}}{\partial x} + \dfrac{\partial\tau_{zy}}{\partial y} + \dfrac{\partial\sigma_z}{\partial z} + f_z + \sigma_{z0} = 0 \end{cases} \quad (22)$$

where $\sigma =$ normal stress; $\tau =$ shear stress; $f =$ body force; $\sigma_0 =$ principal in-situ stress in three dimensions. Integration of the preceding equations over the domain gives the stiffness matrix. Governing equation on continuum medium using integral calculus over a

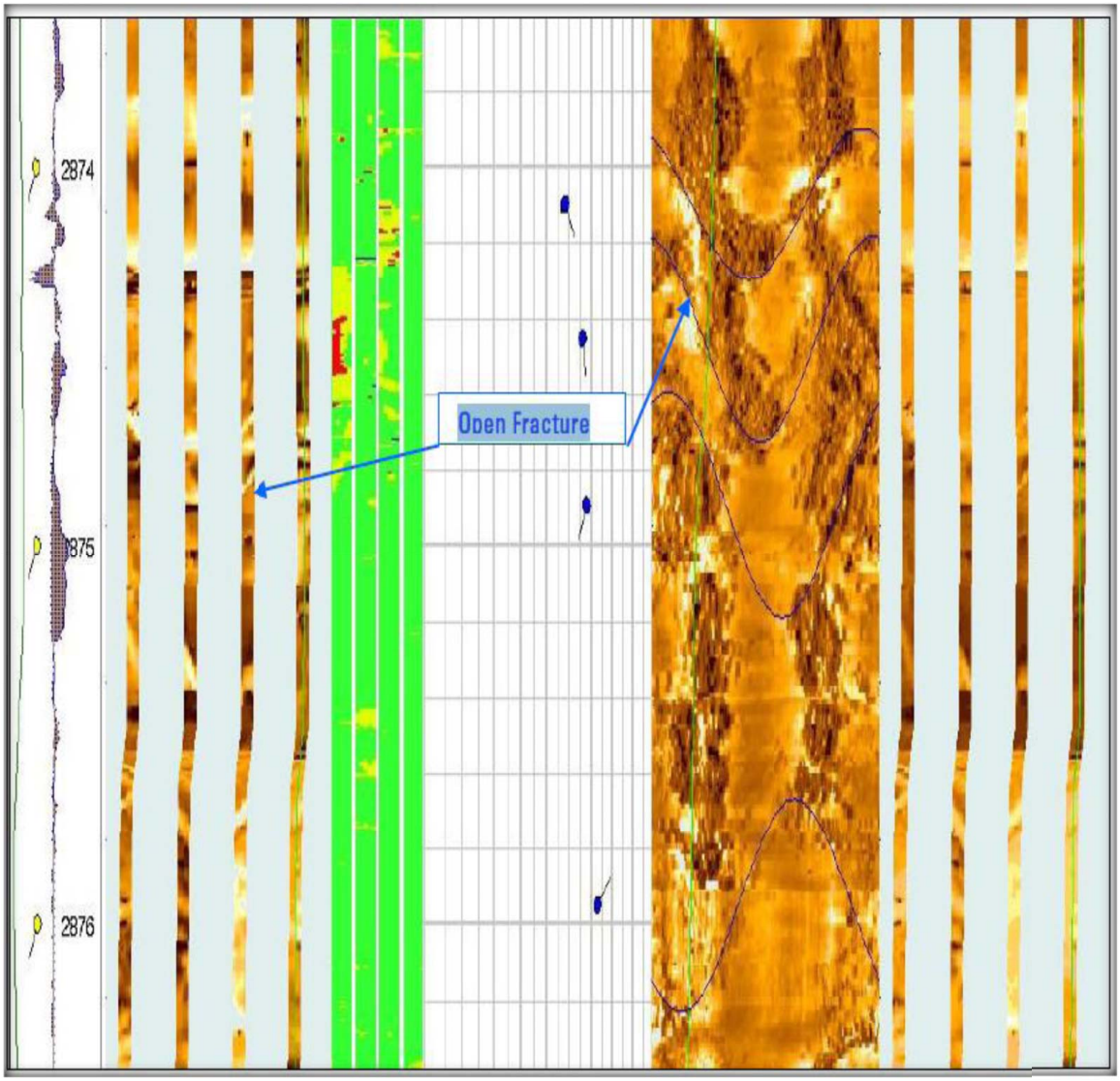

(a)

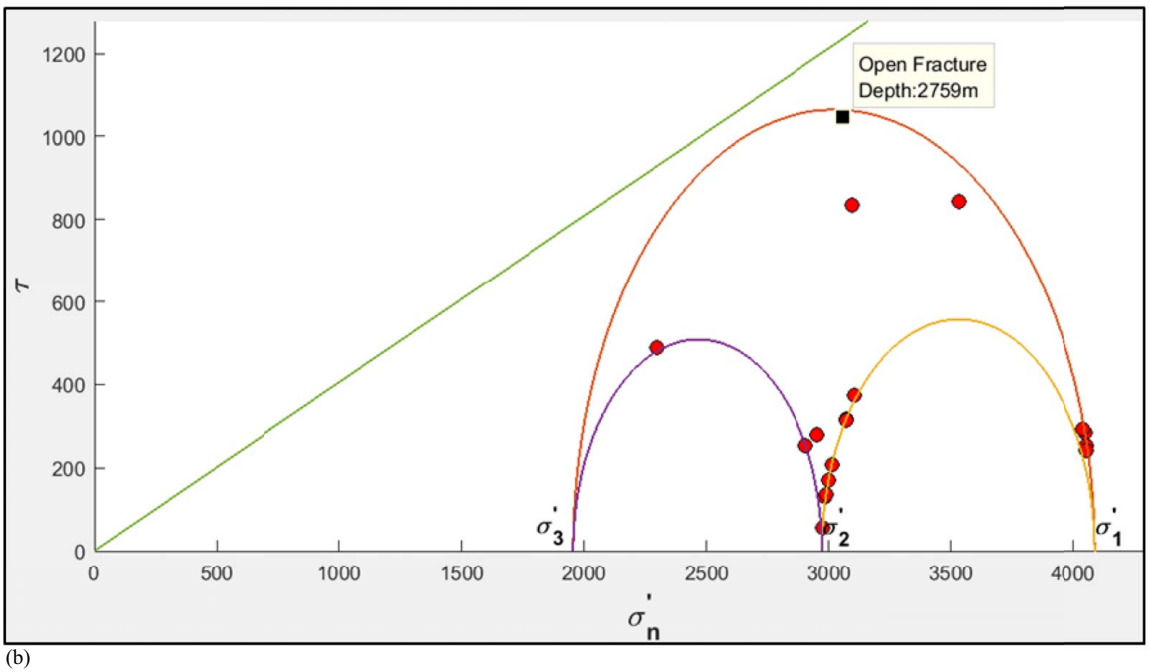

(b)

Fig. 11. Instability potential of different fractures: (a) fractures picked from an OBMI-UBI log; and (b) in the 3D Mohr diagram.

Table 4. Input properties for the fracture stability analysis

No	Dip	Dip azimuth	Type
1	79	239	Open fracture
2	17	192	Unconformable bed
3	7	26	HC bedding
4	7	27	Bedding
5	15	101	Stylolite
6	15	69	Stylolite
7	87	7	Breakout
8	87	7	Breakout
9	87	7	Breakout
10	87	8	Breakout
11	17	14	Unconformable bed
12	85	7	Breakout
13	52	56	Open fracture
14	21	26	Unconformable bed
15	85	9	Breakout
16	85	9	Breakout
17	9	2	HC bedding
18	3	159	Stylolite
19	11	19	Lamination
20	11	20	Lamination
21	55	289	Open fracture
22	68	223	Open fracture

Note: HC = high confidence.

domain can be expressed as

$$\iiint(\sigma_{ij,j} + f_i + \sigma_{i0})dV = 0 \tag{23}$$

Well-known elasticity equation for elastic material is expressed as

$$\{\sigma\} = [C]\{\varepsilon - \varepsilon_0\},$$
$$\{\sigma_0\} = [C]\{\varepsilon_0\} \tag{24}$$

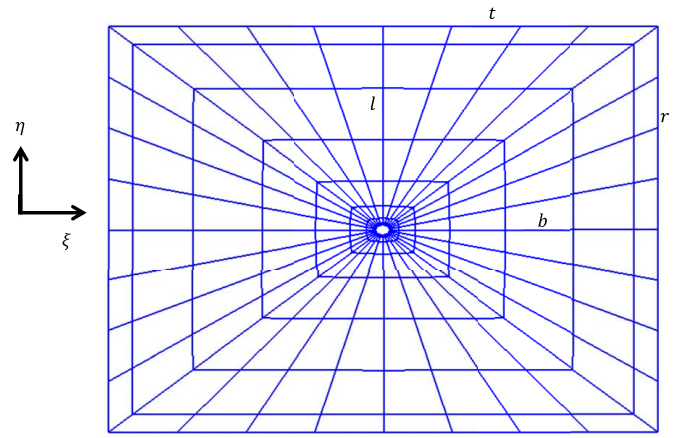

Fig. 13. Mesh generation around the wellbore using transfinite interpolation technique; four boundaries are shown in *l*, *t*, *r*, and *b*.

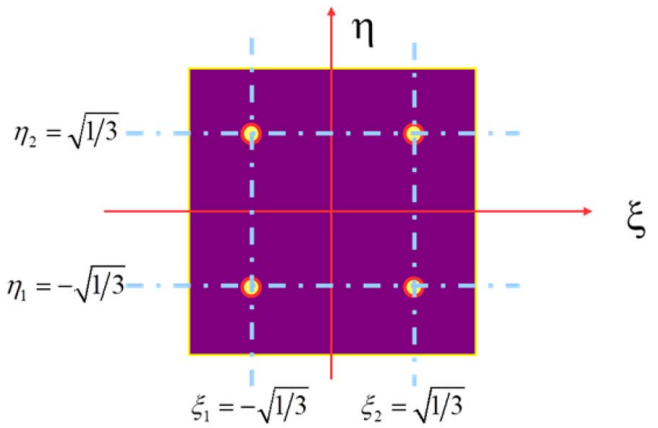

Fig. 14. Two-point rule of Gaussian integration method in the 2D local space.

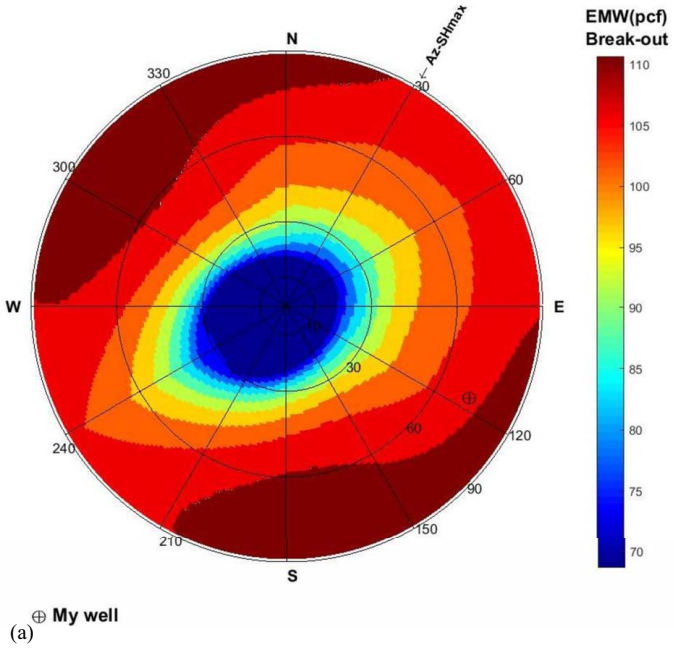

(a)

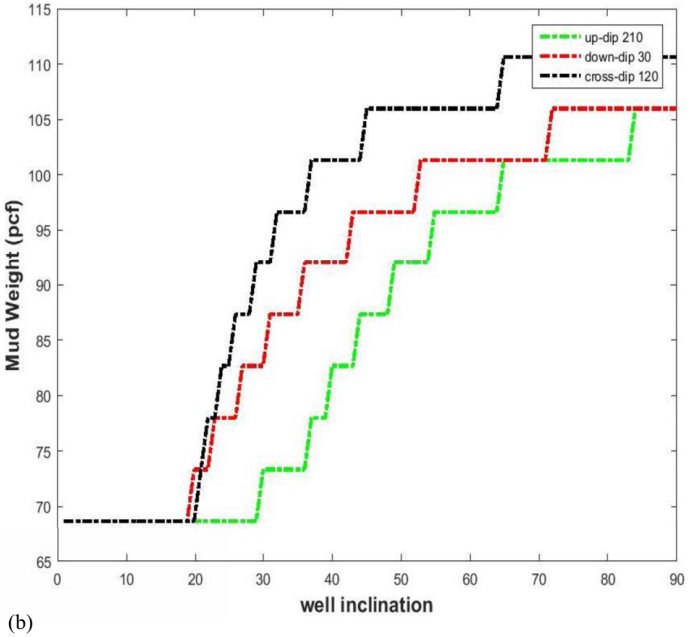

(b)

Fig. 12. (a) Polar plot; and (b) sensitivity analysis of the mud weight in Laffan shale formation at 1,363 mTVD. Input data include: $\nu = 0.29$, $\phi = 30°$, $C = 8$ MPa, $P_p = 15$ MPa, $\sigma_v = 31$ MPa, $\sigma_h = 25$ MPa, $\sigma_H = 28$ MPa, $C_{wp} = 3$ MPa, $\phi_{wp} = 12°$, $\beta_{wp} = 8°$, $\alpha_{wp} = 30°$.

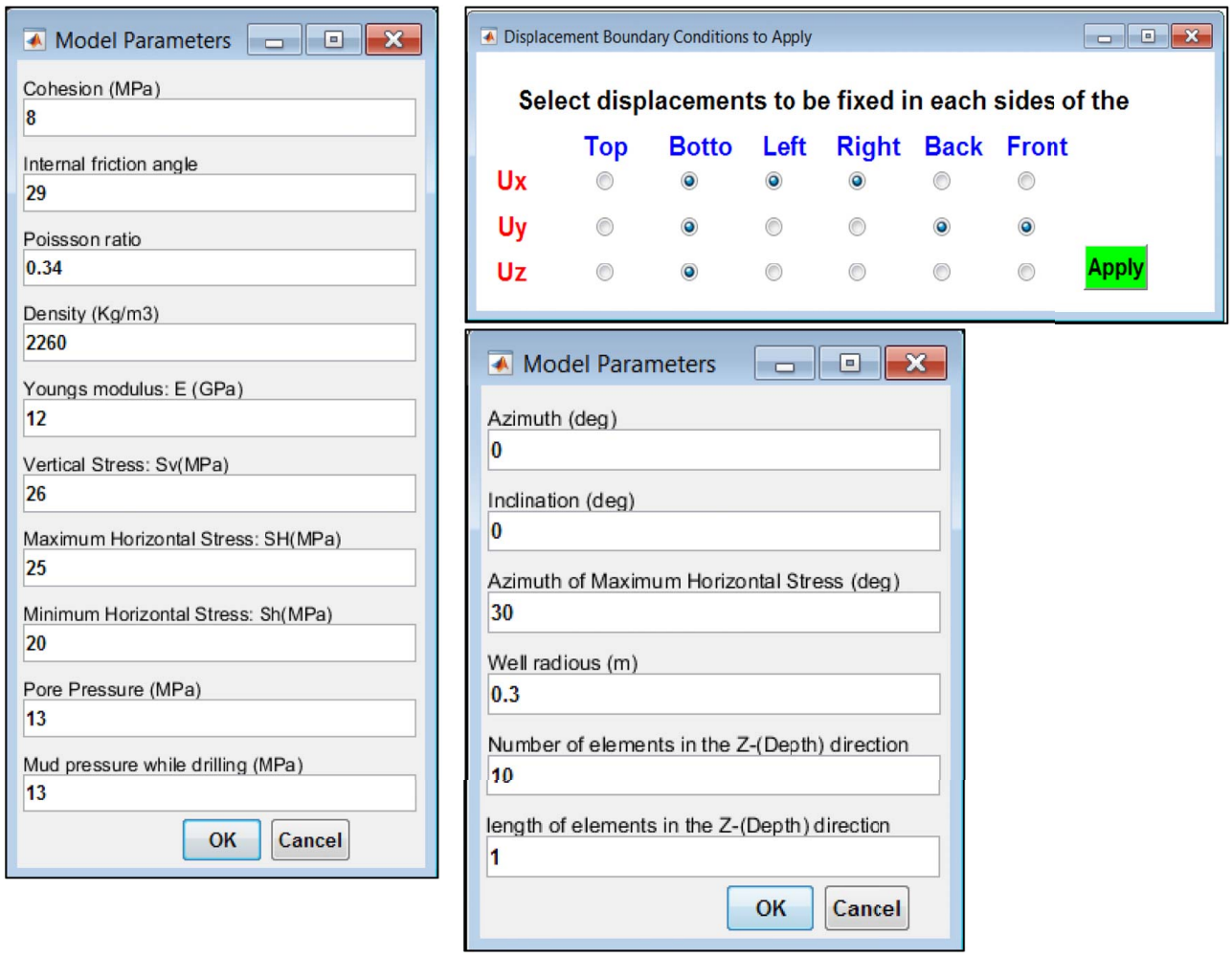

Fig. 15. Input parameters and boundary condition windows of numerical module.

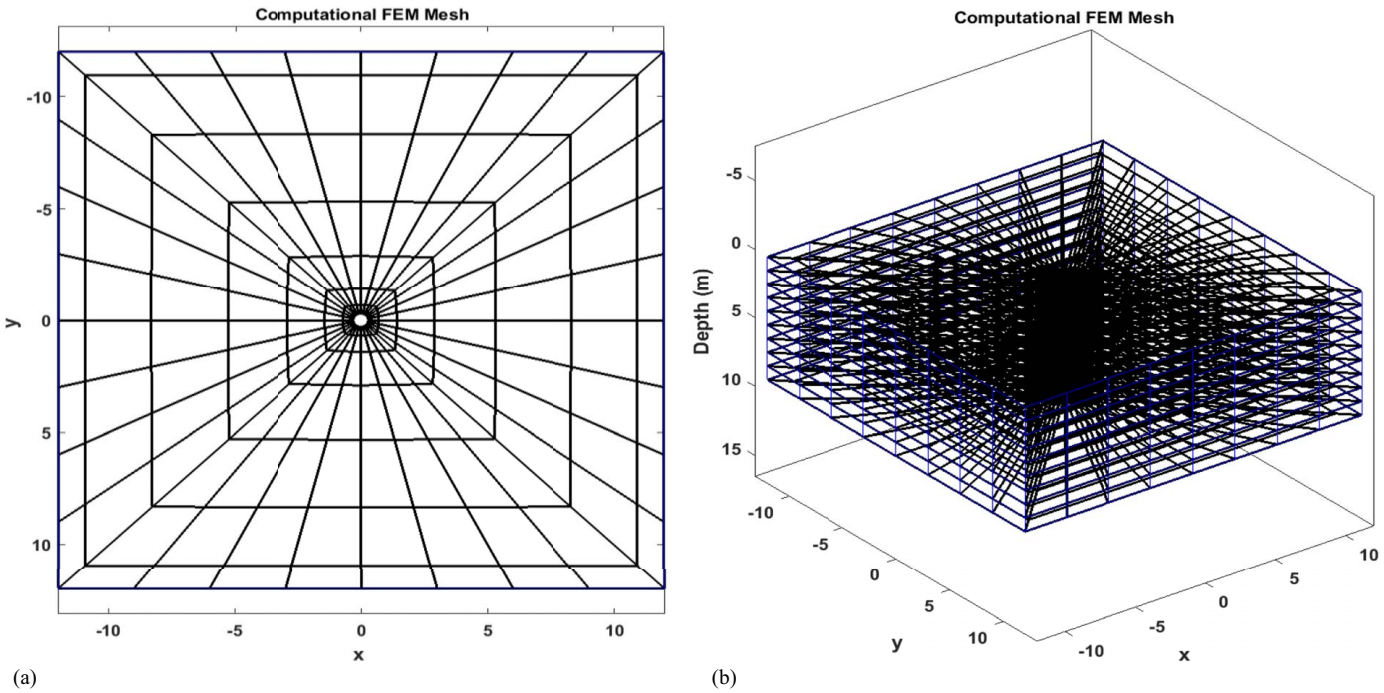

(a) (b)

Fig. 16. Mesh generated around wellbore: (a) top view; and (b) 3D view.

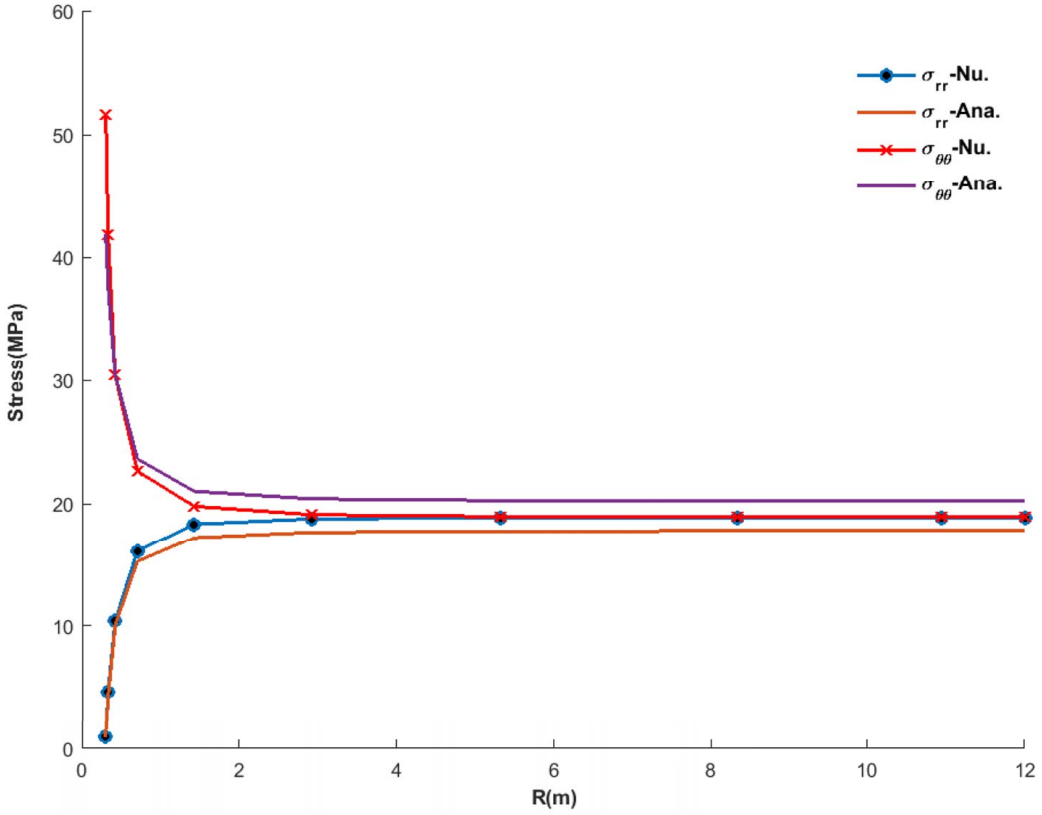

Fig. 17. Numerical and analytical comparison of the tangential and radial stress.

where ε = strain tensor; ε_0 = in-situ strain; and C = elastic matrix for isotropic material in 3D is expressed as

$$[C]=\frac{E}{(1+\nu)(1-2\nu)}\begin{bmatrix} 1-\nu & \upsilon & \nu & 0 & 0 & 0 \\ \nu & 1-\nu & \nu & 0 & 0 & 0 \\ \nu & \nu & 1-\nu & 0 & 0 & 0 \\ & & & \frac{1-2\nu}{2} & 0 & 0 \\ 0 & 0 & 0 & & & \\ 0 & 0 & 0 & 0 & \frac{1-2\nu}{2} & 0 \\ 0 & 0 & 0 & & & \\ & & & 0 & 0 & \frac{1-2\nu}{2} \end{bmatrix} \tag{25}$$

The term ε_0 in stress calculation is ignorable as it is very small in earth considering equilibrium conditions. A strain tensor with six elements is connected to displacements through the following differential equation:

$$\varepsilon=\begin{bmatrix} \frac{\partial N}{\partial x} & 0 & 0 \\ 0 & \frac{\partial N}{\partial y} & 0 \\ 0 & 0 & \frac{\partial N}{\partial z} \\ \frac{\partial N}{\partial y} & \frac{\partial N}{\partial x} & 0 \\ \frac{\partial N}{\partial z} & 0 & \frac{\partial N}{\partial x} \\ 0 & \frac{\partial N}{\partial z} & \frac{\partial N}{\partial y} \end{bmatrix} \tag{26}$$

In the next step, we need to connect displacements to the shape functions (Lagrange function) to convert our calculations from global (physical) to local (computational) space for a hexahedral eight-point element as

$$N_i=\frac{1}{8}(1+\xi_i\xi)(1+\eta_i\eta)(1+\zeta_i\zeta) \tag{27}$$

where N = shape function; and ξ_i, η_i, and ζ_i = coordinates of element nodes at local space. The benefit of this conversion is that all the nodes in local space vary in (−1, 1). To take into account pore pressure at each node of the elements in a porous formation, Terzaghi's effective stress was calculated which is

$$\sigma'_{ij}=\sigma_{ij}-\alpha P p\delta_{ij}+\sigma_0 \tag{28}$$

where σ' = effective stress; σ = total stress; and δ = Kronecker delta. Substituting Eqs. (24)–(28) into Eq. (23) element stiffness matrix is expressed as

$$K_e=\iiint B'CBdV+\iiint \alpha B'PpNdV+\iiint N'bdV+\iiint N'S_ndA + \iiint B'N\sigma_0 dVB=\ [D][N] \tag{29}$$

where K_e = element stiffness matrix; B = derivation of shape function; S_n = traction or the surface forces; and b = body force. To solve the continuous integrals in Eq. (29), the most common method is discrete Gaussian quadrature method (Logan 2012), particularly, with *Legendre* polynomials where by integrating in 3D, it

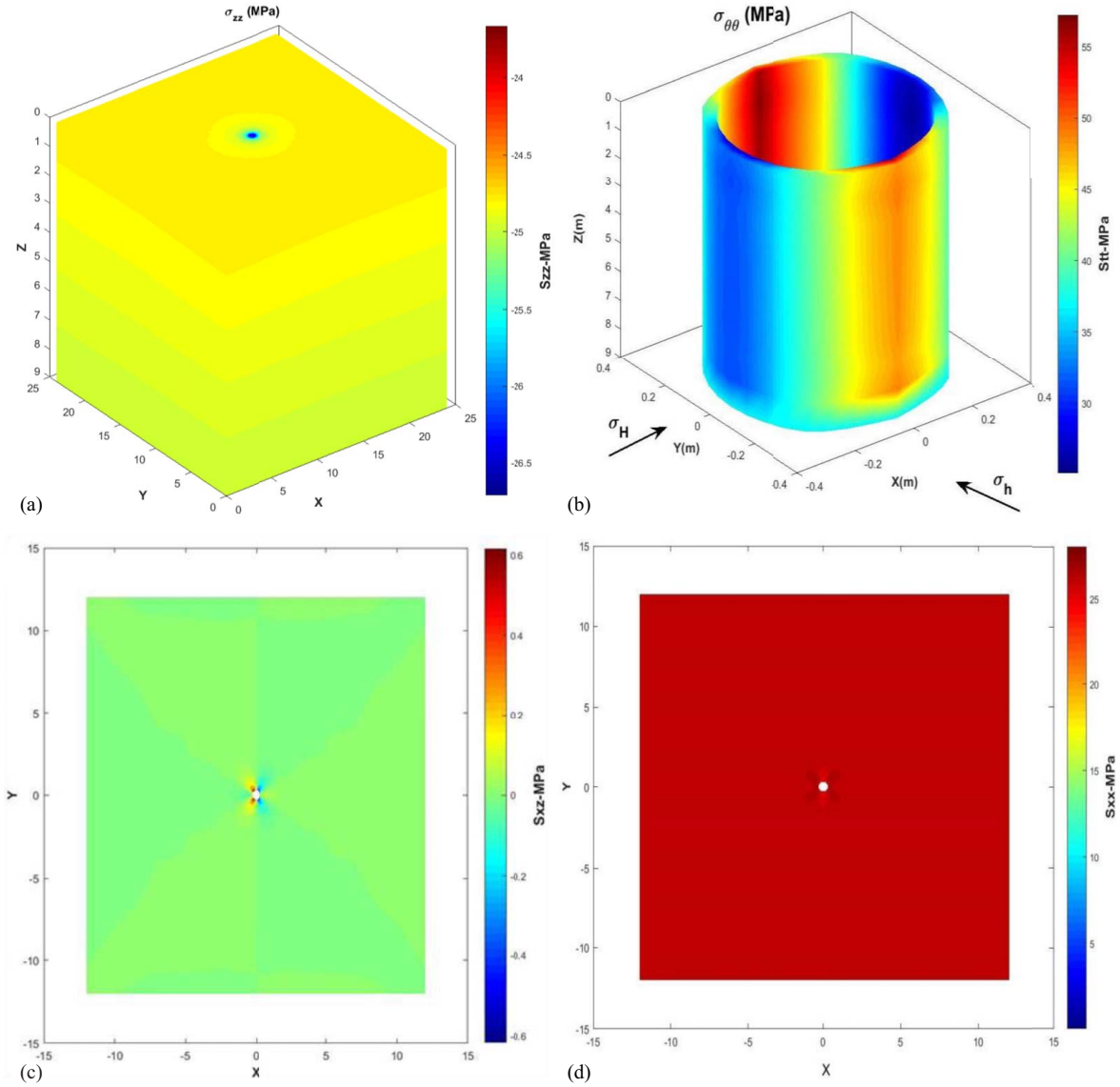

Fig. 18. Stress results in model around wellbore: (a) total stress in *z*-direction; (b) total tangential stress; (c) shear stress in *x*–*z* plane; and (d) total stress in *x*-direction.

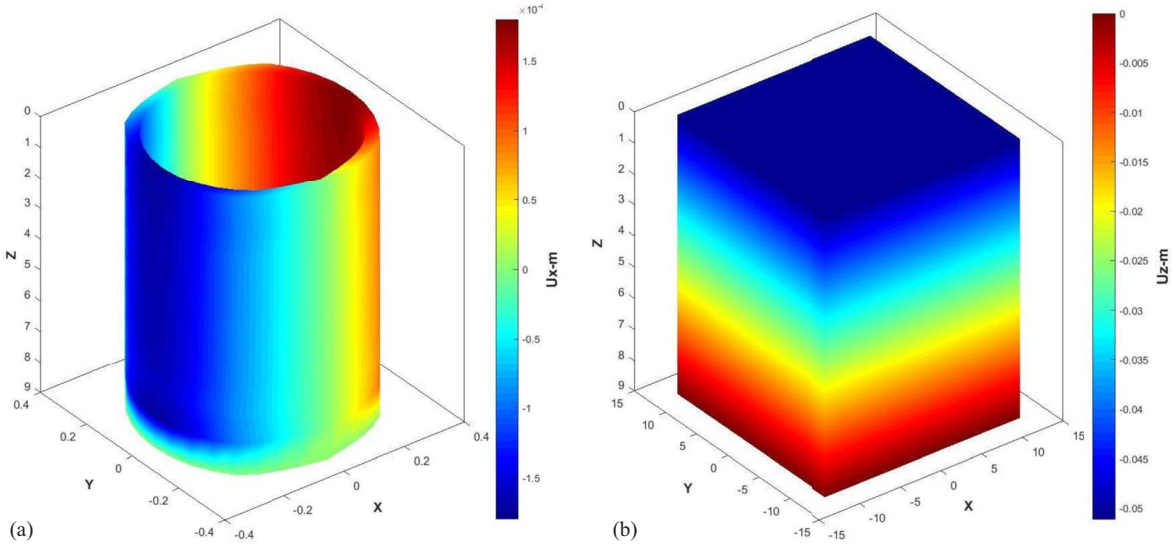

Fig. 19. Displacement results: (a) around wellbore in *x*-direction; and (b) in whole model in *z*-direction.

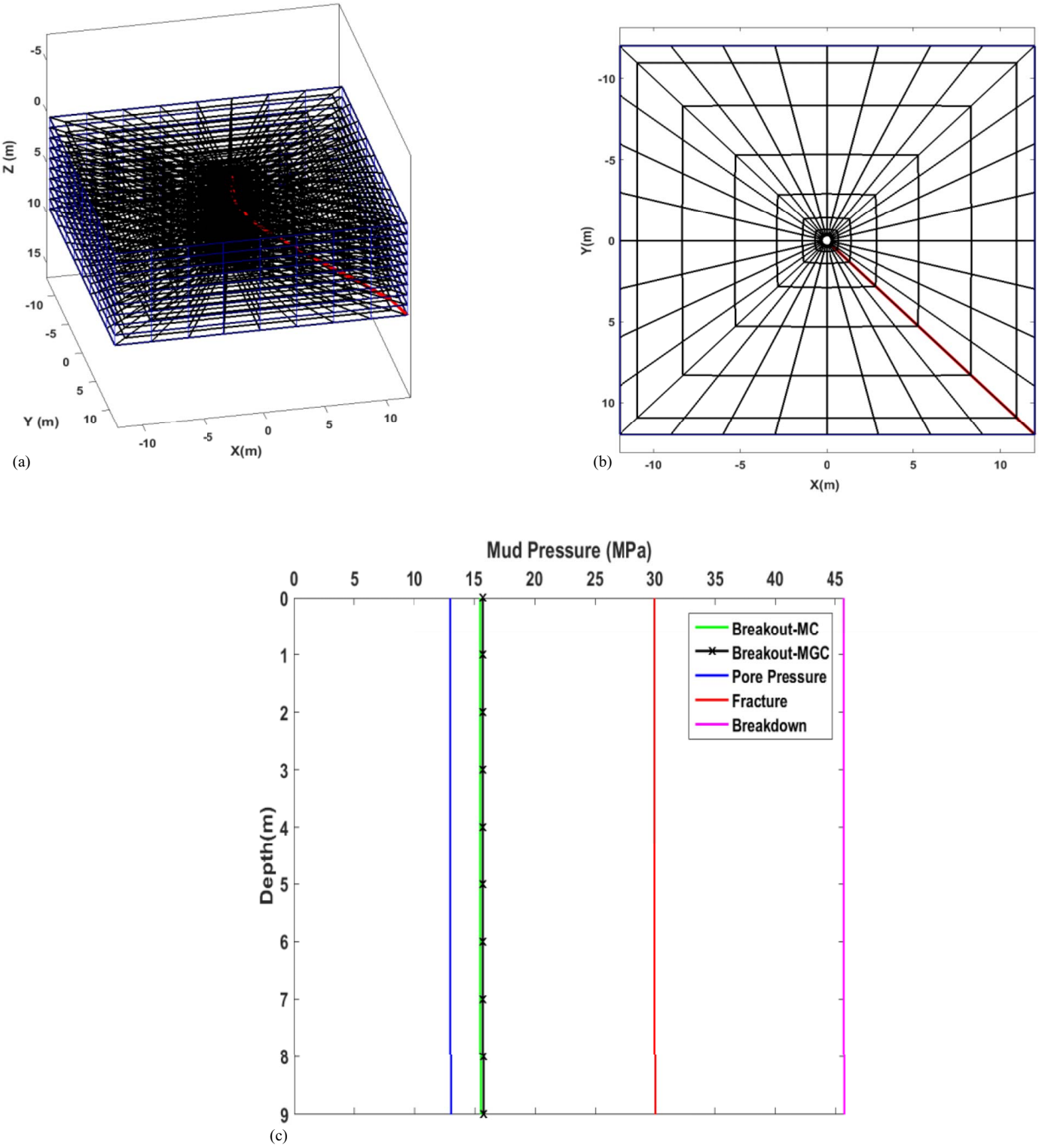

Fig. 20. (a) The new well plan directed to the lower right corner of the model; (b) top view; and (c) mud window predicted from the numerical calculations for the new plan.

becomes

$$\iiint_{-1}^{1} f(\xi, \eta, \zeta) d\xi d\eta d\zeta \approx \sum_{i=1}^{n} \sum_{j=1}^{n} \sum_{k=1}^{n} w_i w_j w_k f(\xi, \eta, \zeta) \quad (30)$$

where $w =$ weight of numerical integration via two-point rule shown in Fig. 14 where in 3D it becomes eight points ($2 \times 2 \times 2$).

In a hexahedral element, a matrix with 24° of freedom in three dimensions is assembled to the neighbor elements based on their connectivity to form the total matrix of the whole model. Finally, solving Eq. (29) using Eq. (30) and substituting into the well-known global stiffness matrix, it becomes

$$Ku = F_b + F_s + F_{is} \quad (31)$$

where u = displacement; F_b = body force; F_p = pore pressure; F_s = traction; and F_{is} = in-situ force. Nodal stress is calculated as

$$\sigma = CBu \tag{32}$$

For element stress calculation, the nodal stresses are averaged over the cube. In addition, boundary condition including fixing displacements of the nodes on the sides and bottom of the model are needed to obtain the full matrix of displacement from Eq. (31). Programming the preceding equations led to the numerical module of the developed program.

Numerical Module Output

In this module, a vertical wellbore in a single formation with properties from Table 3 has been modeled to observe the results of the FE analysis. To model wellbore stress and displacement, Eqs. (21) to (31) have been programmed, and results are described in this section. Fig. 15 shows input data windows, including geometry, boundary conditions, and mechanical properties selected from Table 3 at 1,190 mTVD. Boundary conditions are of two types: stress boundary and displacement boundary, which are crucial to solving the stiffness matrix in Eq. (31). For real boundaries, imposing displacement conditions provide relevant results while stress boundary underestimates stresses and displacements. It should be noted that the model is run in a geostatic equilibrium (steady-state) analysis, not in a time-dependent transient analysis.

The transfinite technique has been used to generate a mesh grid shown in Fig. 16 as described in the section "Mesh Generation." Hexahedral eight-point (brick) elements have been built around the model where, finally, it includes 2,592 elements with 3,200 nodes. Each element is integrated counterclockwise to obtain the element stiffness matrix and assembled with $8° \times 3°$ of freedom to form the total model stiffness matrix with $9{,}600 \times 9{,}600$ arrays. Bottom displacements are fixed in three dimensions, left and right on the x-side of the model; back and front are fixed on the y-side of the model (Fig. 15).

The in-situ stresses are orthogonally applied to the 3D model. They were transformed from the in-situ coordination to the global coordination using Eqs. (11) and (12), that is, σ_H is in the x-direction, σ_h is in the y-direction, and overburden is downward at the top of the model. After applying boundary conditions and running the model, the results were compared with the Kirsch solution (Appendix II). Fig. 17 compares numerical radial and tangential stresses with the analytical stresses. The numerical results nearly matched the analytical model, and the difference could be due to the model's mesh size. In Fig. 18(a), stress contours in the z-direction (σ_{zz}) are shown where total stress obtained is in agreement with applied overburden where it reaches 25.01 MPa at depth by applying 22,170.6 KN/m^3 of the body weight. Shear stress in the x–z plane (σ_{xz}) is shown in Fig. 18(b). As noted, the maximum stress concentration corresponding to the wellbore breakout is in the σ_h direction as seen in Fig. 18(c) around the wellbore. In geostatic equilibrium, computed displacement must be small enough (Logan 2012) as the right term of Eq. (22) is related to density variation over time, which is zero in this analysis. As shown in Fig. 19, vertical and horizontal displacements are small enough of the order of 10^{-3} throughout the model and wellbore wall.

Finally, the objective of a 3D numerical simulation is to predict the predrilling mud weight bounds for a proposed well in any direction inside the cube. Therefore, a well plan is directed to the lower right corner of the cube and the result of mud window predicted from the numerical model are shown in Fig. 20(c). Nodal stresses were picked from the intersection of the well with numerical elements. Radial and tangential stress were obtained and introduced into the Mohr–Coulomb and Mogi–Coulomb criteria to determine the mud weight bounds. The breakout pressures from both criteria matched a cross-marked line. Therefore, with the new well direction, the mud weight required to prevent wellbore breakout at 1,190–1,200 m is 80 pcf, which agrees with the mud window in Fig. 9.

Conclusion

A geomechanics program for wellbore stability analysis has been developed, consisting of two parts: an analytical module, and a numerical module. Required data such as physical well logs, lithology intervals, pressure data, formation well tops, and well survey plans were imported into the analytical module. For calculating mechanical rock properties empirical prediction formulas, in-situ stress the poroelastic plane strain method and pore pressure the Modified Eaton's were used. A LOT is mandatory for stress calculations; however, many drillers skip it because of formation fracturing and consequences; thus, from a plane strain concept and drilling evidence, a set of new equations were solved to obtain the minimum and maximum horizontal strains. Safe mud weight bounds through depth and polar plots using the Mohr–Coulomb and Mogi–Coulomb criteria were shown in different windows. The latter underestimated the minimum mud weight to prevent wellbore breakout. Results of this module have been calibrated with drilling events and ultimately could be used for future drilling plans. The transversely isotropic behavior of shale has been solved using the weak-plane slip method. Results showed how formation isotropy could affect the polar plot of the mud window and made it symmetrical concerning the isotropic formation. In comparison with an industrial program, the results of our program in fracture stability, which are crucial in a reservoir in terms of pressure injection or production, correctly showed fractures normal and shear stress poles inside the 3D Mohr diagram.

The numerical module uses the transfinite technique to generate hexahedral mesh elements around a vertical wellbore. The Stiffness matrix was computed in each element using the Gaussian two-point rule integration and assembled in neighbor elements by element connectivity to form the whole model stiffness matrix. Forces are computed by applied in-situ stress, pore pressure, and body forces. Displacement boundary conditions on the bottom and sides of the model are applied, and solving the global stiffness equation in a geostatic equilibrium condition gives the nodal displacement of the whole model. The displacement obtained is introduced into the stress–strain equation, and the total stress in the model is computed. The numerical model matched the analytical Kirsch model and the results showed a high-stress concentration area around a wellbore, which corresponds to the breakout in the wellbore wall. The small displacement obtained shows the model's accuracy, which is of the order of 10^{-3}, and maximum shear stress observed at the direction of maximum horizontal stress.

Appendix I. Mud Weight Bounds Based on the Rock Failure Criteria

The most common rock failure criteria to determine the mud weight required for stable drilling are the Mohr–Coulomb and the Mogi–Coulomb criteria. The corresponding bounds in the

Mohr–Coulomb are calculated as

$$\begin{aligned}
&\tau = C + \sigma_n \tan(\varphi)\\
&\mathrm{P}_{wb_mc} = \frac{3\sigma_H - \sigma_h + \mathrm{P}_0(N-1) - UCS}{N+1}\\
&N = \frac{1+\sin(\varphi)}{1-\sin(\varphi)}\\
&\mathrm{P}_{wf_mc} = \frac{UCS + N(3\sigma_h - \sigma_H) - \mathrm{P}_p(N-1)}{N+1}
\end{aligned} \tag{33}$$

where P_{wb_mc} = minimum required mud weight to prevent wellbore breakout; and P_{wf_mc} = maximum required mud weight for fracturing the formation based on the Mohr–Coulomb criterion. The Mogi–Coulomb criterion considers the effect of middle principal stress, σ_2, on the rock shear failure along an octahedral plane and like the preceding equation its mud weight bounds are

$$\begin{aligned}
&\tau_{oct} = a + b\sigma_m\\
&\tau_{oct} = \frac{1}{3}\sqrt{(\sigma_1-\sigma_2)^2 + (\sigma_1-\sigma_3)^2 + (\sigma_2-\sigma_3)^2}\\
&\sigma_m = \frac{1}{2}(\sigma_1+\sigma_3)\\
&a = \frac{2\sqrt{2}}{3}c\cos(\varphi),\ \ b = \frac{2\sqrt{2}}{3}\sin(\varphi)\\
&(I_1^2 - 3I_2)^{1/2} = a' + b'(I_1 - \sigma_2 - 2Pp)\\
&I_1 = \sigma_1+\sigma_2+\sigma_3,\ I_2 = \sigma_1\sigma_2 + \sigma_2\sigma_3 + \sigma_1\sigma_3\\
&a' = 2c\cos(\varphi),\quad b' = \sin(\varphi)\\
&\mathrm{P}_{wb_mgc} = \frac{1}{2}A - \frac{1}{6}\sqrt{12(a+b(A-2Pp))^2 - 3(A-2B)^2}\\
&\mathrm{P}_{wf_mgc} = \frac{1}{2}D + \frac{1}{6}\sqrt{12(a+b(D-2Pp))^2 - 3(D-2E)^2}\\
&D = 3\sigma_h - \sigma_H\\
&A = 3\sigma_H - \sigma_h
\end{aligned} \tag{34}$$

where σ_1, σ_2, and σ_3 = principal stresses; I_1, I_2, and I_3 = stress invariants; τ_{oct} = octahedral shear stress; P_{wb_mgc} = minimum required mud weight to prevent the wellbore breakout; and P_{wf_mgc} = maximum required mud weight to fracture the formation.

Appendix II. Kirsch Solution around a Wellbore

The Eq. (22) has been expressed by Kirsch (1898) in the cylindrical coordination as

$$\begin{cases}
\dfrac{\partial\sigma_r}{\partial r} + \dfrac{1}{r}\dfrac{\partial\tau_{\theta r}}{\partial\theta} + \dfrac{\partial\tau_{zr}}{\partial z} + \dfrac{\sigma_r - \sigma_\theta}{r} + f_r = 0\\
\dfrac{1}{r}\dfrac{\partial\sigma_\theta}{\partial\theta} + \dfrac{\partial\tau_{r\theta}}{\partial r} + \dfrac{\partial\tau_{z\theta}}{\partial z} + 2\dfrac{\tau_{r\theta}}{r} + f_\theta = 0\\
\dfrac{\partial\tau_{z\theta}}{\partial z} + \dfrac{\partial\tau_{zr}}{\partial z} + \dfrac{1}{r}\dfrac{\partial\tau_{z\theta}}{\partial\theta} + \dfrac{\tau_{zr}}{r} + f_z = 0
\end{cases} \tag{35}$$

Integrating over the wellbore area with an in-situ stress tensor the following components are calculated:

$$\begin{aligned}
&\sigma_{rr} = \left(\frac{\sigma_x^0+\sigma_y^0}{2}\right)\left(1-\frac{a^2}{r^2}\right) + \left(\frac{\sigma_x^0-\sigma_y^0}{2}\right)\left(1+3\frac{a^4}{r^4}-4\frac{a^2}{r^2}\right)\\
&\cos 2\theta + \sigma_{xy}^0\left(1+3\frac{a^4}{r^4}-4\frac{a^2}{r^2}\right)\sin 2\theta + P_w\frac{a^2}{r^2}\\
&\sigma_{\theta\theta} = \left(\frac{\sigma_x^0+\sigma_y^0}{2}\right)\left(1+\frac{a^2}{r^2}\right) - \left(\frac{\sigma_x^0-\sigma_y^0}{2}\right)\left(1+3\frac{a^4}{r^4}\right)\\
&\cos 2\theta - \sigma_{xy}^0\left(1+3\frac{a^4}{r^4}\right)\sin 2\theta - P_w\frac{a^2}{r^2}\\
&\sigma_{zz} = \sigma_z^0 - \nu\left(2(\sigma_x^0-\sigma_y^0)\frac{a^2}{r^2}\cos 2\theta + 4\sigma_{xy}^0\frac{a^2}{r^2}\sin 2\theta\right)\\
&\sigma_{r\theta} = -\left(\frac{\sigma_x^0-\sigma_y^0}{2}\right)\left(1-3\frac{a^4}{r^4}+2\frac{a^2}{r^2}\right)\\
&\sin 2\theta + \sigma_{xy}^0\left(1-3\frac{a^4}{r^4}+2\frac{a^2}{r^2}\right)\cos 2\theta\\
&\sigma_{\theta z} = (-\sigma_{xz}^0\sin\theta + \sigma_{yz}\cos\theta)\left(1+\frac{a^2}{r^2}\right)\\
&\sigma_{rz} = (\sigma_{xz}^0\cos\theta + \sigma_{yz}\sin\theta)\left(1-\frac{a^2}{r^2}\right)
\end{aligned} \tag{36}$$

where σ_x^0, σ_y^0, and σ_{xy}^0 = in-situ stress components; a = wellbore radius; r = any distance from the wellbore center; and θ is measured from the x-axis.

Data Availability Statement

The following Matlab codes of this program are available upon request from the corresponding author: Geomechanical_Properties.m, Insitu_Stress.m, MC_MW_MultipleDepth.m, MC_MW_SingleDepth.m, Petrophysics.m, SHmax_Stress_Polygon.m, Shear_Velocity.m, Petrophysics.m, Parameters.m, Input_Calc_Model_Parameters.m, Fracture_Slip.m, and read_las.m.

Acknowledgments

The authors want to greatly thank the Iranian Offshore Oil Company for providing well data, laboratory tests, facilities, and opportunity for this research.

References

Al-Ajmi, A. M., and R. W. Zimmerman. 2006. "Stability analysis of vertical wellbores using the Mogi–Coulomb failure criterion." *Int. J. Rock Mech. Min. Sci.* 43: 1200–1211. https://doi.org/10.1016/j.ijrmms.2006.04.001.

Ameen, M. S., B. G. D. Smart, J. M. Somerville, S. Hammilton, and N. A. Naji. 2009. "Predicting rock mechanical properties of carbonates from wireline logs (A case study: Arab-D reservoir, Ghawar field, Saudi Arabia)." *Mar. Pet. Geol.* 26: 430–444. https://doi.org/10.1016/j.marpetgeo.2009.01.017.

Asaka, M., and R. M. Holt. 2021. "Anisotropic wellbore stability analysis: Impact on failure prediction." *Rock Mech. Rock Eng.* 54: 583–605. https://doi.org/10.1007/s00603-020-02283-0.

Azadpour, M., N. ShadManaman, A. Kadkhodaie-Ilkhchi, and M.-R. Sedghipour. 2015. "Pore pressure prediction and modeling using well-

logging data in one of the gas fields in south of Iran." *J. Pet. Sci. Eng.* 128: 15–23. https://doi.org/10.1016/j.petrol.2015.02.022.
Bowers, G. L. 1995. "Pore pressure estimation from velocity data: Accounting for overpressure mechanisms besides undercompaction." *SPE Drill. Complet* 10: 89–95. https://doi.org/10.2118/27488-PA.
Bradley, W. B. 1979. "Failure of inclined boreholes." *J. Energy Res. Technol.* 101: 232–239. https://doi.org/10.1115/1.3446925.
Chen, M., Y. Jin, and G. Q. Zhang. 2008. *Petroleum related rock mechanics*. Beijing: Science Press.
Eaton, B. A. 1975. "The equation for geopressure prediction from well logs." In *Proc., Fall Meeting of the Society of Petroleum Engineers of AIME*. SPE 5544. Dallas, TX: Society of Petroleum Engineers (SPE).
Eissa, E. A., and A. Kazi. 1988. "Relation between static and dynamic young's moduli of rocks." *Int. J. Rock Mech. Min. Sci. Geomech. Abstr.* 25: 479–482. https://doi.org/10.1016/0148-9062(88)90987-4.
Elkatatny, S., M. Mahmoud, I. Mohamed, and A. Abdulraheem. 2018. "Development of a new correlation to determine the static Young's modulus." *J. Pet. Explor. Prod. Technol.* 8: 17–30. https://doi.org/10.1007/s13202-017-0316-4.
Elyasi, A., and K. Goshtasbi. 2015. "Numerical modeling of the stability of horizontal multidrain oil wells." *China Ocean Eng.* 29: 719–732. https://doi.org/10.1007/s13344-015-0075-2.
Fjaer, E., R. M. Holt, P. Horsrud, A. M. Raaen, and R. Risnes. 2008. *Petroleum related rock mechanics*. 2nd ed. Amsterdam, Netherland: Elsevier.
Ghoreishian Amiri, S. A., S. A. Sadrnejad, and H. Ghasemzadeh. 2017. "A hybrid numerical model for multiphase fluid flow in a deformable porous medium." *Appl. Math. Modell.* 45: 881–899. https://doi.org/10.1016/j.apm.2017.01.042.
Gutierrez, M. A., N. R. Braunsdore, and B. A. Couzens. 2006. "Calibration and ranking of pore-pressure prediction models." *Leading Edge* 25: 1516–1523. https://doi.org/10.1190/1.2405337.
Hawkes, C. D., S. P. Simth, and P. J. McLellan. 2002. "Coupled modeling of borehole instability and multiphase flow for underbalanced drilling." In *Proc., of IADC/SPE Drilling Conf.* SPE-74447-MS. Dallas, TX: Society of Petroleum Engineers (SPE).
Horsrud, P. 2001. "Estimating mechanical properties of shale from empirical correlations society of petroleum engineers." *SPE Drill. Complet* 16 (2): 68–73. https://doi.org/10.2118/56017-pa.
ISRM (International Society for Rock Mechanics). 2007. "The complete ISRM suggested methods for rock characterization, testing and monitoring: 1974–2006." In *Suggested methods prepared by the commission on testing methods*, edited by R. Ulusay, and J. A. Hudson, 57–94. Ankara, Turkey: ISRM, Compilation Arranged by the ISRM Turkish National Group.
Jaeger, J. C. 1960. "Shear failure of anistropic rocks." *Geol. Mag.* 97 (1): 65–72. https://doi.org/10.1017/S0016756800061100.
Jaeger, J. C., N. G. W. Cook, and R. W. Zimmerman. 2007. *Fundamentals of rock mechanics*. 4th ed. Hoboken, NJ: Blackwell Publishing.
Kidambi, T., and G. S. Kumar. 2016. "Mechanical Earth Modeling for a vertical well drilled in a naturally fractured tight carbonate gas reservoir in the Persian Gulf." *J. Pet. Sci. Eng.* 141: 38–51. https://doi.org/10.1016/j.petrol.2016.01.003.
Kirsch. 1898. "Die Theorie der Elastizität und die Bedürfnisse der Festigkeitslehre." *Zeitschrift des Vereines deutscher Ingenieure* 42: 797–807.
Lee, H., S. H. Ong, M. Azeemuddin, and H. Goodman. 2012. "A wellbore stability model for formations with anisotropic rock strengths." *J. Pet. Sci. Eng.* 96–97: 109–119. https://doi.org/10.1016/j.petrol.2012.08.010.
Leseikin, V. D. 2010. *Grid generation methods*. 2nd ed. Berlin: Springer.
Li, B., R. C. K. Wong, B. Xu, and B. Yang. 2018. "Comprehensive stability analysis of an inclined wellbore embedded in Colorado shale formation for thermal recovery." *Int. J. Rock Mech. Min. Sci.* 110: 168–176. https://doi.org/10.1016/j.ijrmms.2018.07.019.
Li, X., C. Zhang, Y. Feng, Y. Wei, X. Chen, H. Weng, and J. Deng. 2022. "An integrated geomechanics approach to evaluate and manage wellbore stability in a deep graben formation in Tarim basin." *J. Pet. Sci. Eng.* 208: 109391. https://doi.org/10.1016/j.petrol.2021.109391.
Liu, X., W. Zeng, L. Liang, and M. Lei. 2016. "Wellbore stability analysis for horizontal wells in shale formations." *J. Nat. Gas Sci. Eng.* 31: 1–8. https://doi.org/10.1016/j.jngse.2016.02.061.
Logan, D. L. 2012. *A first course in the finite element method*. 5th ed. Boston: Cengage Learning.
Ma, T., and P. Chen. 2015. "A wellbore stability analysis model with chemical-mechanical coupling for shale gas reservoirs." *J. Nat. Gas Sci. Eng.* 26: 72–98. https://doi.org/10.1016/j.jngse.2015.05.028.
MathWorks. 2009 *Discover the latest MATLAB and simulink capabilities at MATLAB EXPO 2023*. Natick, MA: MathWorks.
Molaghab, A., M. H. Taherynia, S. M. Fatemi Aghda, and A. Fahmifar. 2017. "Determination of minimum and maximum stress profiles using wellbore failure evidences: A case study—a deep oil well in the southwest of Iran." *J. Pet. Explor. Prod. Technol.* 7: 707–715. https://doi.org/10.1007/s13202-017-0323-5.
Morley, C. K., R. King, R. Hillis, M. Tingay, and G. Backe. 2011. "Deepwater fold and thrust belt classification, tectonics, structure and hydrocarbon prospectivity: A review." *Earth-Sci. Rev.* 104: 41–91.
Setiawan, N. B., and R. W. Zimmerman. 2018. "Wellbore breakout prediction in transversely isotropic rocks using true-triaxial failure criteria." *Int. J. Rock Mech. Min. Sci.* 112: 313–322. https://doi.org/10.1016/j.ijrmms.2018.10.033.
Tingay, M. R. P., R. R. Hillis, R. E. Swarbrick, C. K. Morley, and A. R. Damit. 2009. "Origin of overpressure and pore-pressure prediction in the Baram province, Brunei." *AAPG Bull.* 93 (1): 51–74. https://doi.org/10.1306/08080808016.
Wu, B., S. K. Choi, and C. P. Tan. 2005. "Effect of stress anisotropic on cavity strength and implications in wellbore stability and sand production analyses. Alaska Rocks 2005." In *Proc., 40th U.S. Symp. On Rock Mechanics*. Anchorage, AK: USRMS.
Xu, S. S., A. F. Neito-Samaniego, and S. A. Alaniz-Alvarez. 2010. "3D mohr diagram to explain reactivation of pre-existing planes due to changes in applied stresses." In *Rock stress and earthquakes*, 38–85. London: Taylor & Francis Group.
Zhang, J. 2011. "Pore pressure prediction from well logs: Methods, modifications, and new approaches." *Earth Sci. Rev.* 108: 50–63. https://doi.org/10.1016/j.earscirev.2011.06.001.
Zoback, M. D. 2007. *Reservoir geomechanics*. New York: Cambridge.
Zoback, M. D., C. A. Barton, M. Brudy, D. A. Castillo, T. Finkbeiner, B. R. Grollimund, D. B. Moos, P. Peska, C. D. Ward, and D. J. Wiprut. 2003. "Determination of stress orientation and magnitude in deep wells." *Int. J. Rock Mech. Min. Sci.* 40: 1049–1076. https://doi.org/10.1016/j.ijrmms.2003.07.001.